Customized nonlinearity shaping in imperfect or variable waveguides

by

Jérémy Kelly-Massicotte

A thesis
presented to the University of Waterloo
in fulfillment of the
thesis requirement for the degree of
Masters degree
in
Physics (Quantum Information)

Waterloo, Ontario, Canada, 2019

Author's Declaration

I hereby declare that I am the sole author of this thesis. This is a true copy of the thesis, including any required final revisions, as accepted by my examiners.

I understand that my thesis may be made electronically available to the public.

Abstract

Generation of high-quality single photons via heralded parametric downconversion requires careful design of spectral correlations in down-converted photon pairs. One step in this design process involves customized engineering of ferroelectric domains. In this thesis, we explore two aspects of such customized domain engineering.

We first explore the impact of fabrication imperfections on two main domain engineering methods, by simulating domain variations in domain engineered structures. We quantify the impact by calculating the purity and amplitude of the generated photon. We conclude that realistic fabrication imperfections do not impair purity and amplitude significantly for the studied methods. However, high variations of the dispersion relations in the crystal impact purity and amplitude significantly.

We then introduce two new domain engineering methods designed for mediums with varying dispersion relations. The first is a generalization of an existing algorithm used to design the domain configurations. The second method relies on varying the domain sizes. We show that the first method yields modest improvement, while the second one works remarkably well, even in conditions with extreme change in dispersion.

Acknowledgements

First and foremost, I want to thank Agata M Brańczyk, who went above and beyond to help me succeed in my graduate studies. Not only did her advice helped me become a better scientist, but also a better human all around. I am really grateful for all the opportunities she has offered to me.

Thanks to Eugene Adjei and Fatih Dinç for helping me improve the horrible talks that you had to sit through, and for sharing scientific ideas.

I would like to thank Kevin Resch and his group for allowing me to join their weekly journal club. This has been an inestimable help in improving my communication abilities. It has also been a great experience to learn science through them.

I also want to acknowledge the amazing hospitality of Christine Silberhorn and her group members, who welcomed me in their offices for a few months. I've met truly inspiring, brilliant people including Michael Stefsky, Matteo Santandrea, Vahid Ansari, Thomas Nitsche, Jano Gil López and Marcello Massaro, who welcomed me and allowed me to learn a lot from them.

And thanks to my advising committee composed of Rajibul Islam, Christine Muschik and Donna Strickland, and to Norbert Lütkenhaus for reviewing my thesis and attending my defense.

Finally, thanks to my girlfriend Ish who supported me through my whole degree, et merci à ma famille et à mes parents Sharon et André qui ont été d'un support moral essentiel à mon succès. Je vous aime.

Table of Contents

List of Figures

Chapter 1

Introduction

Single photons are ideal carriers of quantum information. The generation of high purity single photons is indispensable for quantum technologies. Quantum experiments such as quantum cryptography [1], quantum state teleportation [2], quantum metrology [14], require interference between photons. Photons with low purity are undesirable as they don't interfere well. This leads to a lowered quantum behaviour of light, such as a reduced photon bunching effect in Hong-Ou-Mandel interference [22].

Heralded parametric downconversion is the most common source of single photon currently used in experiments, but it has the intrinsic property of creating spectrally mixed, i.e not spectrally pure, photons. Filtering the spectrum of photons coming out of parametric downconversion can be used to reduce this, however filters also bring undesirable side effects, such as photon-number mixing, as will be discussed in Section 2.3.3. An alternative way to lower mixedness of the photon states without these side effects is to engineer the properties of the material used to achieve parametric downconversion. In the last few years, a few methods based on customization of ferroelectric domains inside nonlinear crystals were proposed to do this [4], [17], [10], [11], [33], [8].

Engineering the material properties require a high precision during the fabrication process, and is bound to be impacted by imperfections. A benchmark of how these imperfections affect the proposed methods is essential to know how reliable they are under realistic conditions. Also, the proposed methods have been designed under the condition that the dispersion relation in the materials was constant. For future applications where this is not the case, a theoretical understanding of how photons with high separability can be generated in materials with varying dispersion is required.

This thesis will first introduce in Chapter 2 the theoretical background required to understand parametric downconversion and the separability of its photons. Chapter 3 will then explore the effect of fabrication imperfections on the domain engineering methods, through numerical simulations of its effects. We will then discuss in Chapter 4 two theoretical models we have developed which can be used to manipulate the parametric downconversion light spectrum in materials with dispersion relations, and the outcome of numerical simulations of these methods.

Chapter 2

Theory

In this chapter, we will introduce the necessary theoretical background to understand the research presented in the next chapters. We will introduce the most popular way to generate quantum light, known as parametric downconversion (PDC)[1], and describe in detail the spectral distribution of photon pairs generated using PDC. We will cover how electric poling can be used to customize the shape of the joint spectrum of photon pairs. We will then show this can be applied to an important problem in quantum optics: the generation of spectrally pure single photons.

2.1 Nonlinear Optics

As light travels through media, there are inevitable interactions that occur between the two. The mere fact of light travelling through air, instead of vacuum, slows it down by an astonishing 300,000 km/h. Light can interact linearly with material, which means its optical field strength is interacting linearly with its environment. Moreover, light can also interact nonlinearly, giving rise to higher-order powers of the electric field as the factor mediating interactions.

---

[1] PDC is also often referred to as spontaneous parametric downconversion (SPDC)

Light interaction with material comes from its capacity to induce a change in the dipole moments of atoms in proximity, leading to an overall induced polarization $\vec{P}(t)$, that we can describe as a power series expansion of the electric field $\tilde{E}(t)$ [3]:

$$\vec{P}(t) = \epsilon_0(\chi^{(1)}\vec{E}(t) + \chi^{(2)}\vec{E}^2(t) + \chi^{(3)}\vec{E}^3(t) + ...), \tag{2.1}$$

with $\chi^{(n)}$ referred to as the nth order nonlinear optical susceptibility, or nth order nonlinear coefficient. Because of the fact that this polarization is present in the electric displacement field $\vec{D}(t)$ [19]:

$$\vec{D}(t) = \epsilon_0\vec{E}(t) + \vec{P}(t), \tag{2.2}$$

and the displacement itself in the wave equation of the electric field inside of the material,

$$\nabla \times \nabla \times \vec{E}(t) + \mu_0 \frac{\partial^2}{\partial t^2}\vec{D}(t) = 0, \tag{2.3}$$

it means that the induced polarization will reintroduce nonlinear electric field components in the medium. This allows, as an example among many, second harmonic generation, in which a fraction of the pump present in the medium combine into light with twice the energy.

Similarly, if the polarization is described using quantized electric fields, nonlinear interaction leads to the creation of fields coming from the induced polarization through the Hamiltonian description of the electric field [7]:

$$H_{EM} \propto \int dr^3 E(r,t) \cdot D(r,t). \tag{2.4}$$

Some processes described by this interaction between quantized fields simply have no classical counterparts; they are purely quantum mechanical phenomena. Parametric down-conversion, the main pillar of this work, is an example of such a quantum-only nonlinear effect. It is the mechanism by which one photon gets separated into two photons with lower energy, and is one of the most effective ways to generate single photons, via a process known as heralding.

2.2 Parametric Down-Conversion

Parametric down-conversion is the quantum mechanical process by which a photon of frequency ω_p, coming from a pumping source in a nonlinear material gets converted into a pair of photons called the idler and signal, with respective frequencies ω_i and ω_s. The process is illustrated on Figure 2.1, happening left-to-right.

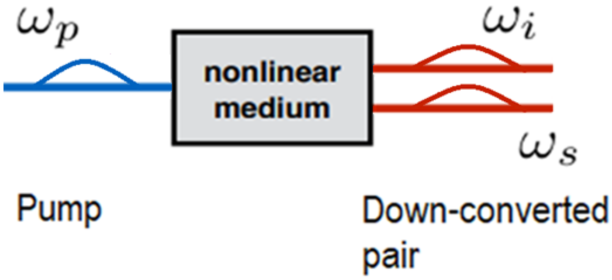

Figure 2.1: Parametric downconversion illustration.

PDC is often described in a regime where we approximate the pumping field as undepleted, given that the strength of the interaction is relatively low, thus converting only a small fraction of the pump. The pump is also considered as behaving classically, as it is assumed that the crystal is pumped with a relatively strong laser, which can be described with classical optics. However, in order to see the effect appear, the electric field for the output fields has to be quantized. In the case where light is confined in a one-dimensional waveguide of length L, the Hamiltonian description of PDC ($\hat{H}_{PDC}$), including the electric fields of the pump $E_p^{(+)}$, the idler $\hat{E}_i^{(-)}$, and the signal $\hat{E}_s^{(-)}$ is the following [7]:

$$\hat{H}_{PDC} \propto \chi^{(2)} \int_0^L dz E_p^{(+)}(z,t) \hat{E}_s^{(-)}(z,t) \hat{E}_s^{(-)}(z,t) + h.c, \tag{2.5}$$

where z is the longitudinal position in the waveguide. The PDC Hamiltonian induces the transformation of a vacuum state into a superposition of a vacuum state, a two photon pair term and terms with higher order pairs, in the ω_i and ω_s modes. While higher order terms can be desirable for certain applications, for the purpose of this work, we will focus on the two-photon component, which is a valid approximation for most applications, as long as the pump brightness is not too high [7]. To the first order in photon pairs of the perturbation expansion of the PDC Hamiltonian, this leads to the following (not normalized) description of the PDC state:

$$|\psi\rangle_{PDC} = |0\rangle_{\omega_s} |0\rangle_{\omega_i} + C \int\int d\omega_s d\omega_i f(\omega_s, \omega_i) a^\dagger_{\omega_i} a^\dagger_{\omega_s} |0\rangle_{\omega_s} |0\rangle_{\omega_i}, \tag{2.6}$$

with $a^\dagger_{\omega_n}$ representing the creation operator acting on the mode ω_n, and C representing a constant grouping physical constants $\frac{i\epsilon_0}{2\hbar}$, with ϵ_0 as the vacuum permittivity, and $\hbar$ as the Planck constant. As we can see from Equation (2.6), the creation operators acting on the vacuum state have a distribution that is dictated by a function that depends on the two generated photon frequencies, $f(\omega_s, \omega_i)$. This means that the generated photons amplitude for a given mode pair, which once squared represents the probability of finding those photons for a given pump input, will depend on the two photon frequencies in a codependent way. This function is referred to as the joint-spectral amplitude (JSA), and it contains the energy and momentum conservation boundaries of the conversion process.

The two physical restrictions composing the JSA are expressed as two functions of the generated photons and are respectively called the pump envelope function (PEF) (noted $\alpha(\omega_s+\omega_i)$) and phasematching function (PMF) (noted $\Phi(\omega_s, \omega_i)$). The product of the PEF and the PMF results in the JSA.

$$f(\omega_i, \omega_s) \equiv JSA \equiv PMF \times PEF \equiv \Phi(\omega_s, \omega_i)\alpha(\omega_s + \omega_i), \tag{2.7}$$

these functions will be discussed in upcoming sections. Different types of parametric downconversion can happen in material, each characterized by a set of polarization orientations for the three interacting PDC photons. In this work we will focus on type-II PDC, in which the pump photons have the same polarization as the idlers, and both have an orthogonal polarization to the signal photons.

An exceptional feature of parametric downconversion is contained in the fact that photons are created in pairs. Detection of a single photon in one polarization mode heralds the presence of another single photon in the other polarization mode. But correlations in the JSA are equivalent to spectral entanglement of the photons in the pair. As we will see in Section 2.2.4, entanglement can impair the separability of the photons and is undesirable when generating single photons, because it reduces the spectral purity of the heralded photon. However, there are ways in which the PDC process can be controlled to prevent entanglement, as will be discussed in Section 2.3.3.

2.2.1 Pump Envelope Function

The pump envelope function comes from the shape of the spectral distribution of a light source incoming in the nonlinear medium. It dictates the energy conservation of the conversion of photons from the pump. Pulsed laser sources used as pumps for PDC typically would be generating ultra-short pulses with a $sech^2(t/\tau)$ temporal shape, but analytically, replacing it with a Gaussian temporal shape (Equation (2.8)) has a marginal effect on the calculation purity and amplitude [16]. For simplicity, we will treat the pumps as Gaussian functions in the present work. By doing so and using a Gaussian spectral distribution centered at $\bar{\omega}_p$, with a standard deviation σ_p, the PEF can be expressed in the following way:

$$PEF \equiv \alpha(\omega_s + \omega_i) = \exp\left\{ -\frac{(\bar{\omega}_p - \omega_s - \omega_i)^2}{\sigma_p^2} \right\}, \tag{2.8}$$

Figure 2.2 shows what a typical pump envelope function for a Gaussian laser looks like, for the two downconverted photons (ω_i & ω_s) amplitudes.

2.2.2 Phasematching Function

The phasematching function comes from the conservation of momentum inside the material. It is written in the following way:

$$PMF \equiv \Phi(\omega_s, \omega_i) = \int_0^L \chi^{(2)}(z) e^{i\Delta k(\omega_s,\omega_i)z} dz \tag{2.9}$$

where L is the physical length of the medium in which the photons are interacting, $\chi^{(2)}(z)$ the second-order nonlinearity coefficient for a position z in the medium, and $\Delta k(\omega_s, \omega_i)$ is

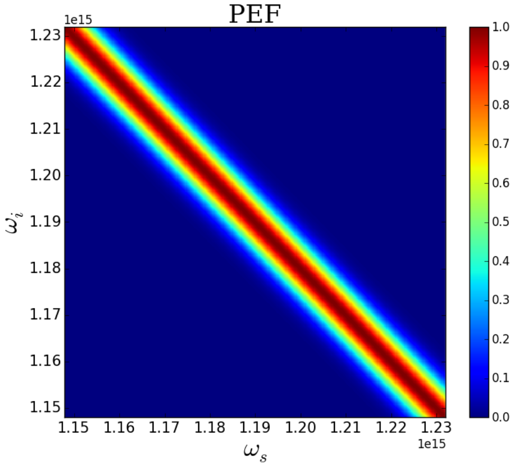

Figure 2.2: Pump envelope function for a central wavelength of 1310 nm, and a $0.1\%\bar{\omega}_p$ standard deviation.

the phase mismatch for a frequency pair. Phase mismatch is the difference in momentum of the three photons involved in PDC:

$$\Delta k(\omega_i, \omega_s) = k_p(\omega_i + \omega_s) - k_i(\omega_i) - k_s(\omega_s), \tag{2.10}$$

and allow the manipulation of the shape of the PMF. The PMF can be controlled in various ways. The cross sectional-shape of the PMF is determined by the Fourier transform of $\chi^{(2)}(z)$, and a longer waveguide gives a more narrow cross-section. The position (in downconverted frequency space) of the PMF is given by the zeroth order term of Δk, while the gradient of the PMF (in downconverted frequency space) is given by the first order term of Δk. Customizing the gradient of the PMF is known as group-velocity matching. An example of a phasematching function is shown on Figure 2.3.

2.2.3 Group-velocity matching

Group velocity matching enable the possibility to change the orientation of the PMF. We saw on Figure 2.3 that a diagonal PMF was possible, but every orientation is possible

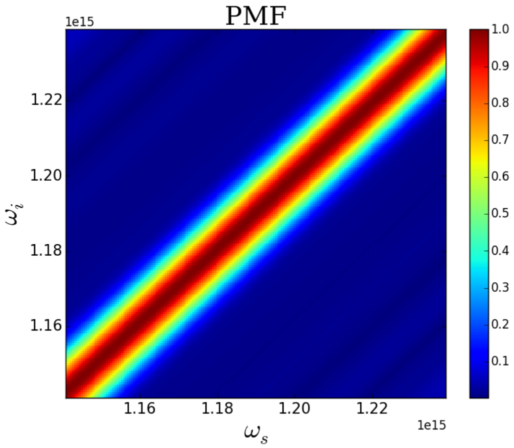

Figure 2.3: Phasematching function for a 44.6mm long crystal.

through group-velocity matching. It works by selecting a frequency for the pump whose group velocity matches certain conditions in regards to those of the signal and idler, as we will show.

Refractive index in the material depends on the temperature of the material and the frequency of the light travelling through it. The refractive index frequency dependency is an empirical formula given by the Sellmeier's equations (see Appendix A for more details). The link between the wavenumber and the frequency inside a crystal with refractive index n is given by:

$$k(\omega) = \frac{\omega n(\omega)}{c}. \tag{2.11}$$

As mentioned previously, in type-II PDC, pump photons polarized along either axis of the material and the second one is orthogonal to it. In a birefringent material with two orthogonal axis of different refractive index, it imply that the pump and the idler photon will travel through one refractive index ($n_x(\omega)$) and the signal through a different one ($n_y(\omega)$). Assuming that we have type-II PDC, Equation (2.10), can then be written:

$$\Delta k(\omega_i, \omega_s) = \frac{\omega_p n_x(\omega_i + \omega_s)}{c} - \frac{\omega_s n_y(\omega_s)}{c} - \frac{\omega_i n_x(\omega_i)}{c}. \tag{2.12}$$

Expanding Equation (2.12) in a Taylor series around the central frequency of the pump $2\bar{\omega}$, which leads to degenerate photons at $\omega_i = \omega_s = \bar{\omega}$ and truncating at the first order in $\bar{\omega}$ gives:

$$\begin{aligned}\Delta k(\omega_i, \omega_s) = \frac{n_x(\omega_i + \omega_s)(\omega_i + \omega_s)}{c}|_{2\bar{\omega}} - \frac{n_x(\omega_i)\omega_i}{c}|_{\bar{\omega}} - \frac{n_y(\omega_s)\omega_s}{c}|_{\bar{\omega}} \\ + \frac{(\omega_s + \omega_i - 2\bar{\omega})}{V_{g_p}} - \frac{(\omega_i - \bar{\omega})}{V_{g_i}} - \frac{(\omega_s - \bar{\omega})}{V_{g_s}},\end{aligned} \tag{2.13}$$

where V_{g_p}, V_{g_i} and V_{g_s} respectively are the group-velocities of the pump, idler and source photons at their central frequency, and $\bar{\omega}$ is half of the central frequency of the pump.

By selecting a pump frequency leading to the condition $V_{g_p} = \frac{V_{g_s} + V_{g_i}}{2}$, the output PMF is a diagonal distribution that opposes the pump's one (see Figure 2.4a)). As we can see, this comes from the shape of the $\Delta k(\omega_i, \omega_s)$; the PMF orientation mimics the orientations of the Δk function. Another example of a group velocity matched PMF is show on the right side of Figure 2.4, where the group velocity of the idler and signal are matched, giving an horizontal PMF.

The oppositely oriented diagonal of the symmetrical PMF leads to a symmetrical JSA along the top-left bottom-right diagonal, having a symmetric group-velocity matching is an essential condition in order to generate indistinguishable photons in PDC pairs, as an asymmetrical joint-spectral amplitude leads to a widely different spectral distribution for the measurement of the individual photons. In order to have truly indistinguishable photon, the side lobes we see on the JSA's of Figure 2.4 also need to be eliminated using a more elaborate engineering of the crystal, as we will see in Section 2.3.2.

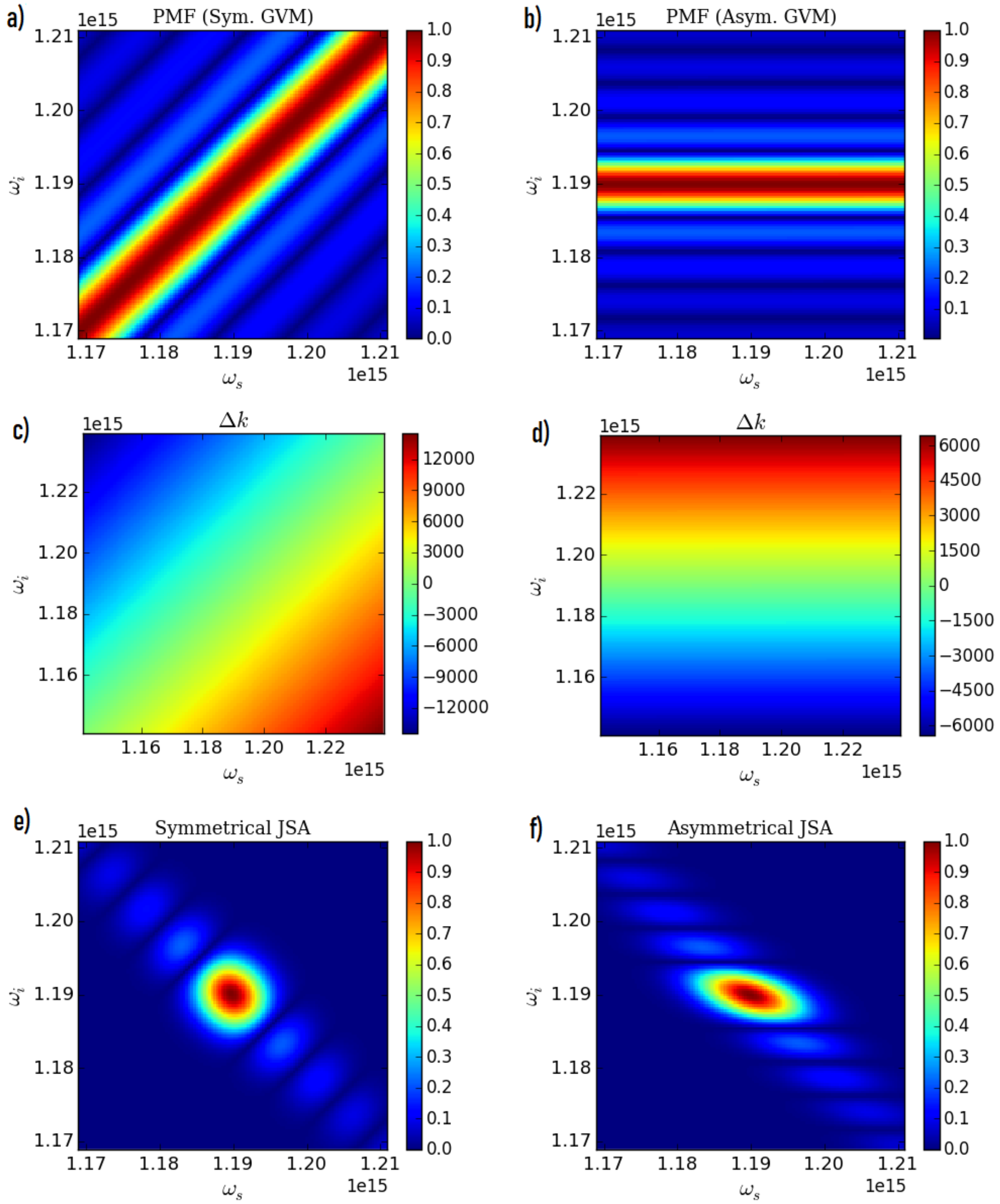

Figure 2.4: JSA, PMF and Δk distributions resulting from symmetrical a), c) & e) and asymmetrical b), d) & f) group-velocity matching for a 4.46mm periodically poled KTP crystal.

2.2.4 Photon purity

Purity quantifies of how mixed a given quantum state is, it is defined as $P = \mathrm{Tr}\{\rho^2\}$. Low purity leads to a loss of the quantum properties of the light, diminishing the interference effect. High purity of single photon is therefore essential in order to use them for quantum information applications.

Entanglement between two systems leaves each individual system in a mixed state. Before discussing this notion for photons, which are infinite dimensional, let's first discuss this for a simple two-level system, i.e a qubit. For example, if we take a two qubit Bell state, which is a maximally entangled two-qubit state,

$$\Phi_+ = \frac{|00\rangle + |11\rangle}{\sqrt{2}}, \tag{2.14}$$

and we discard the first qubit, the remaining one is left in a statistical mixture of basis states:

$$\hat{\rho} = \mathrm{Tr}_1\left(\Phi_+\Phi_+^\dagger\right) = \frac{1}{2}\begin{pmatrix} 1 & 0 \\ 0 & 1 \end{pmatrix}. \tag{2.15}$$

The purity of this state is $P = \frac{1}{2}$, which is the minimum for a qubit. However, if we look at an unentangled state,

$$\Psi = \alpha\,|00\rangle + \beta\,|01\rangle\,, \tag{2.16}$$

where $|\alpha|^2 + |\beta|^2 = 1$ and throw away the first qubit, we get:

$$\hat{\rho} = \mathrm{Tr}_1\left(\Psi\Psi^\dagger\right) = \frac{1}{2}\begin{pmatrix} \alpha\alpha^* & \alpha\beta^* \\ \alpha^*\beta & \beta\beta^* \end{pmatrix}. \tag{2.17}$$

The purity of this state is 1, which is the maximum possible purity for a quantum state. We can see that to have a pure state, we want our bipartite system to be unentangled.

To discuss the relationship between purity and entanglement for more complicated systems, it is useful to introduce the Schmidt decomposition. Schmidt decomposition is defined as the decomposition of a bipartite state in a sum of tensor products of vectors in the subspaces:

$$\Psi = \sum_{i=0}^{N} c_i \left| n_i \right\rangle \left| m_i \right\rangle , \tag{2.18}$$

where c_i represents the Schmidt coefficients, and $\left| n_i \right\rangle$ and $\left| m_i \right\rangle$ are orthogonal vectors in the first and second subspace. If we calculate the Schmidt decomposition of the unentangled state in Equation (2.16), we get

$$\Psi = \left| 0 \right\rangle \otimes (\alpha \left| 0 \right\rangle + \beta \left| 1 \right\rangle). \tag{2.19}$$

Since the state is perfectly separable, this gives only one Schmidt coefficient of $c_0 = 1$. However, the Bell state from Equation (2.14) require two Schmidt coefficients, both equal to $\frac{1}{\sqrt{2}}$.

We can rewrite purity as the sum of the fourth power of the normalized Schmidt decomposition coefficients:

$$P = \sum_{i=0}^{N} c_i^4. \tag{2.20}$$

As we can see, a single Schmidt coefficient of $c_0 = 1$ also leads to a purity of 1, and the maximally entangled state leads to a purity of $\frac{1}{N}$, where N is the dimension of the Hilbert space of the state. In order to get high purity photons from PDC photon pairs, we must reduce entanglement. A fully separable JSA which can be expressed as $f(\omega_i, \omega_s) = h(\omega_s) g(\omega_i)$ only has one term in the decomposition, so it leads to an unmixed state once the idler photon is measured. For a general JSA, we can write the Schmidt decomposition:

$$f(\omega_i, \omega_s) = \sum_{k} c_k h_k(\omega_s) g_k(\omega_i). \tag{2.21}$$

From this, we can compute the purity of each photon. The only way to eliminate all spectral correlations, and yield a separable JSA, is to engineer both a Gaussian PEF and a Gaussian PMF [30]. As we will see in the following section, this can be enabled by using domain engineering.

2.3 Quasi-phasematching

Quasi-phasematching is a process in which the sign or magnitude of the nonlinearity of the material is changed periodically [13]. This process allows a high conversion rate from the pump to the two-photon state in PDC by limiting the destructive interference caused by the difference in phase of the pump and generated photons.

To see how it works, let's look back at the PMF equation:

$$\Phi(\omega_i, \omega_s) = \int_0^L \chi^{(2)}(z) e^{i\Delta k(\omega_i,\omega_s)z} dz. \tag{2.22}$$

If we assume that $\chi^{(2)}(z)$ is constant in the material, then Equation (2.22) becomes an integral over a complex oscillating function of spatial frequency (or inverse wavelength) $\frac{\Delta k(\omega_i,\omega_s)}{2\pi}$. The integral in (2.22) will thus be limited to:

$$|\Phi(\omega_i, \omega_s)| \leq \left| \frac{\chi^{(2)}}{\Delta k(\omega_i, \omega_s)} \right|. \tag{2.23}$$

If $\Delta k(\omega_i, \omega_s)$ happens to naturally be close to zero for a frequency pair in a material, the integral will be reduced to:

$$\Phi(\omega_i, \omega_s) = \chi^{(2)} \int_0^L dz = \chi^{(2)} L, \tag{2.24}$$

giving an amplitude that scales with crystal length. This condition can sometimes be met in certain materials, such as Beta Barium Borate (BBO), and when they are, the conversion process is called phasematched. A phasematched process leads to the highest possible conversion efficiency in a material. In spite of this, in most nonlinear materials, this condition does not happen at desired frequencies, or sometimes never happens, and the best option is to achieve quasi-phasematching.

2.3.1 Periodic poling

Quasi-phasematching can be reached if the $\chi^{(2)}(z)$ sign is reversed periodically at every position at for which the complex function starts decreasing. This distance is called the coherence length (L_c), and is half of the inverse of the spatial frequency:

$$L_c = \frac{\pi}{\Delta k(\omega_i, \omega_s)}. \tag{2.25}$$

Applying this periodic reversal to a crystal is referred to as periodic poling, and is illustrated in Figure 2.5f). It is used to maximize the amplitude in the conversion process of PDC at the degenerate, central pump frequency. An example of the JSA obtained from the application of periodic poling on a crystal is shown on Figure 2.4e).

It's worth mentioning, as this convention will be used for the rest of this work, that the position dependent nonlinear coefficient $\chi^{(2)}(z)$ is often expressed in a different way to simplify calculations. Since the domain reversal only changes the sign of the nonlinear coefficient, it can be expressed as $\left|\chi^{(2)}\right| g(z)$ where $g(z)$ takes a +1 or -1 value. The $\left|\chi^{(2)}\right|$ is merged with the C constant from Equation (2.6). We therefore rewrite the PMF using that convention for future reference as:

$$\Phi(\omega_i, \omega_s) = \int_{-\infty}^{\infty} g(z) e^{i\Delta k(\omega_i, \omega_s) z} dz. \tag{2.26}$$

2.3.2 Electric poling

Ferroelectric poling was discovered and experimented on for the first time in 1993, by Yamada, M. et al.[34]. It was proposed as a method to achieve quasi-phasematching in LiNbO$_3$. Electric poling is what allows, in general, quasi-phasematching of nonlinear processes in ferroelectric materials.

Ferroelectric materials have the property that they can have their permanent polarization reversed by an applied external electric field [23]. This means that Equation (2.1) switches sign permanently in the material after the electric field is applied. It is possible to have this effect happen locally by using a localized electrode to force a sign reversal under a locally applied electric field. Such regions are referred to as poled domains. Figure 2.5 illustrates the process of the polarization reversal using electric poling. Domains of electrically poled regions gradually grow due to field exposition to expand away from the electrode.

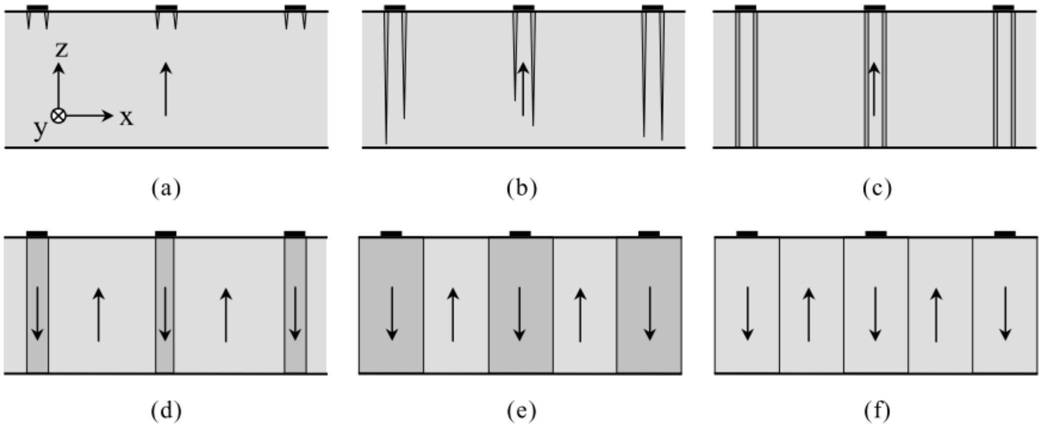

Figure 2.5: Progression of the domain nucleation using electric poling. a) to c) creation of a nucleated region under the applied electric field. d) to f) reversal of the permanent polarization of the region and expansion away from the electrode. Figure was taken from [26].

2.3.3 Non conventional quasi-phasematching

Despite being used in many experiments for its ability to generate single photons, periodic poling has limitations in this regard; photons generated from it have a limited purity. As we can see from the plot of the periodic poling JSA in Figure 2.4e), there are side lobes along the diagonal, which as mentioned in Section 2.2.4, makes the individual photons lose purity. To eliminate the side lobes, we want to generate a Gaussian PMF. This problem can be circumvented by modifying the poling orientations or the domain size. The modification of these properties of a structure is what we call domain engineering.

Instead of domain engineering, experiments often make use of bandpass filters on the JSA to achieve near-unity purity, since it allows the restriction of the spectral range of the generated photons to a small, Gaussian band. However, this simultaneously induce false-detections of pairs, since heralded photons can end up filtered. This leads to false positives in which a photon is expected but not present. Additionally, filters conducive to high purity significantly reduce intensity of heralded pairs [27]. An alternative way to do this that avoids these problems is to engineer the PMF at the source.

To get a Gaussian PMF, a Gaussian nonlinear profile is required [4]. This can be seen by taking the inverse Fourier transform of Equation (2.26) to get the nonlinear profile $g(z)$:

$$g(z) = \int_{-\infty}^{\infty} \Phi(\omega_i, \omega_s) e^{-i\Delta k(\omega_i,\omega_s)z} d\Delta k. \tag{2.27}$$

From Figure 2.4, we saw that under symmetric group-velocity matching, $\Delta k(\omega_i, \omega_s)$ was constant along the orientation of the PMF, but it can be noted that it also varies linearly in the opposite direction diagonal. Therefore a PMF that is a Gaussian function in the diagonal opposite to the pump in the ω_i and ω_s space is also a Gaussian function in the $\Delta k(\omega_i, \omega_s)$ space. The optimal PMF to reach high purity also happens to be a Gaussian in the $\Delta k(\omega_i, \omega_s)$ space, and since the Fourier transform of a Gaussian is also a Gaussian function, the $g(z)$ profile giving optimal purity is also Gaussian. As we noted at the beginning of Section 2.3.2, $g(z)$ can only take discrete +1 or -1 values, so in practice having a Gaussian nonlinearity profile is not possible.

Fortunately, different proposals to mimic the behaviour of a Gaussian $g(z)$ profile have been submitted in the last years. The first proposal comes from [4] by increasing the periodicity of the poling gradually in the shape of a Gaussian function. Another method we will refer to as duty-cycle customization, came from [10]. By increasing the duty-cycle, which is the ratio of poled to unpoled region in a poling period, in a Gaussian way, the $g(z)$ is given an effective Gaussian shape. This is different from the other methods ([4], [33],[12], and [17]), that we will refer to as customized domain orientation. Customized domain orientation methods use aperiodic poling to reach an effective Gaussian nonlinearity profile. Figure 2.6 shows a schematic representation of these poling methods.

Figure 2.7 shows a side-by-side comparison of a JSA created from periodic poling and from customized poling. As we can see, the custom poled crystal generate a more concen-

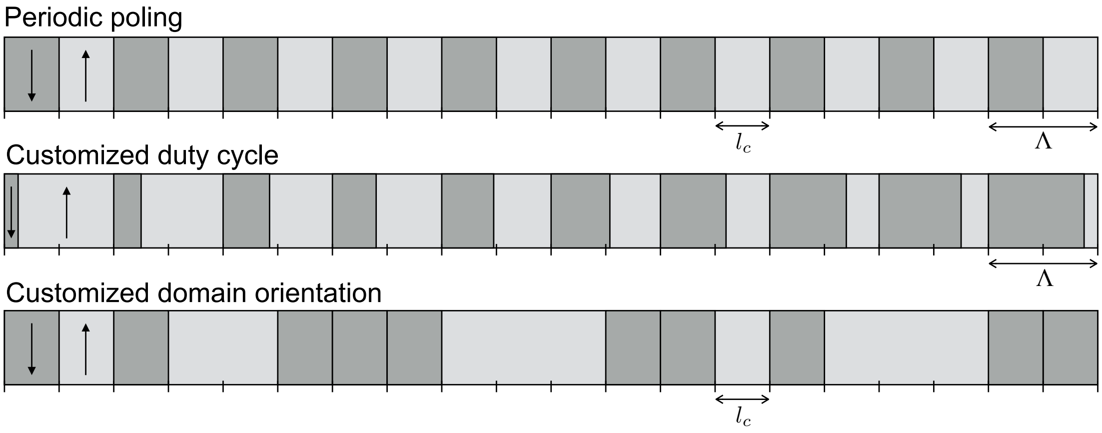

Figure 2.6: Three different domain engineering methods, with Λ showing the poling period.

trated Gaussian with no side lobes. This is translated in the purity, which is 84.5% for the periodically poled crystal and 99.9% for the custom poled one.

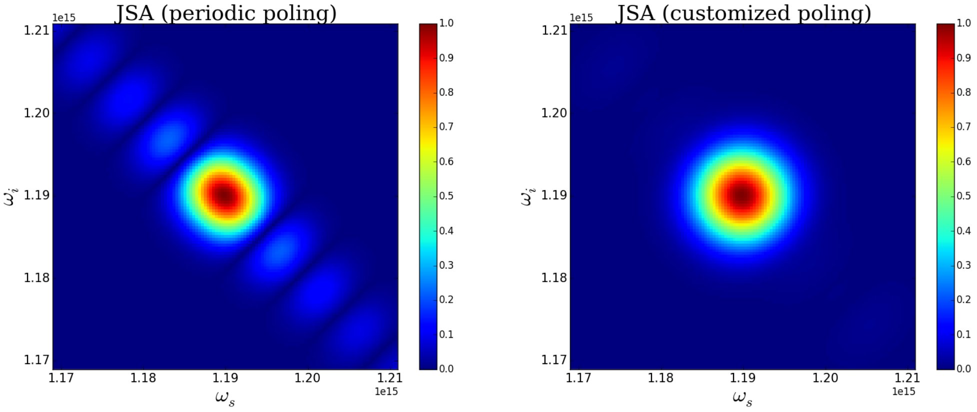

Figure 2.7: JSA of a periodically poled (left) and custom poled (right) 4.46mm KTP crystal.

Chapter 3

Fabrication imperfections in nonlinearity shaping using custom poling

3.1 Introduction

In the previous chapter, we introduced domain engineering methods for the purpose of designing a Gaussian PMF. Understanding how well these methods achieve their goal under various fabrication imperfections in crystal is critical.

When crystals are fabricated and their domains ferroelectrically engineered, they exhibit different types of imperfections. The exact process of how poling will be achieved depends on many factors, including the time of exposure to the field, the size of pieces of patterned photoresists stopping the conduction of the field from one end to the crystal, and the crystal thickness [26]. It is also clear, when looking at microscope imaging of periodically poled crystals, that the domain boundaries are not as precisely positioned as they are in theory.

Recent experiments using domain-engineered crystals to achieve Gaussian PMF have used both duty-cycle methods of nonlinear shaping ([6],[5]) and customized domain orientation methods ([15],[32]). However, at the time the experiments were done, the methods were implemented without literature about the characterization of those imperfections. The research presented in this chapter was motivated by the need to have such a characterization, for the benefit of potential future applications where near-unity purity photons applications will be required.

We've investigated the effect of domain position imperfections on purity and amplitude of down-converted photons on a few different poling techniques. These two metrics were taken because purity is essential for quantum interference for photon and high amplitude is related to photon production rate, which is desirable in experiments. Four types of imperfections that could affect domain positions were determined to represent realistic-case scenarios, namely:

1. **Overpoling and underpoling of regions:** since the size of domains depends on the time of exposure to the field, there is the possibility of a systematic change in the size of all poled domains if there is an uncertainty on the time. Since the electric field is applied uniformly, the size of all domains are affected equally.

2. **Missed domains when poling:** Especially in the case of the duty-cycle method where domain size can be very small, there is a possibility that two subsequently poled domains to merge together and form a single one. There is also the possibility that, in the stage where nucleation sites propagates from one face to the other some domains fail to do so; experiments have show that same samples that produced domains that had not propagated completely from one crystal face to the other also produced domains that did propagate through. ([26] section 2.1.2.3)

3. **Randomized variations in wall positions:** position and orientations of the electrodes used to generate domains can be away from their expected position. This leads to slightly randomized domain positions. This is well known to reduce performance of periodically poled crystals and methods exist to measure the standard deviation of the position of domain walls. [13]

4. **Variation in dispersion relations:** variations on the geometry of a waveguide, or its local temperature can influence the dispersion relations inside the crystal. These

changes of dispersion impact the phase mismatch (Equation 2.12). Correlated noise on dispersion relations has been shown to impact the conversion efficiency in $LiNbO_3$ waveguides [31].

The imperfections, applied to an hypothetical periodically poled structure are shown in Figure 3.1. We perform the analysis of these imperfections in periodically poled and two method involving different ways to achieve a Gaussian PMF: duty-cycle customization from [10] and the poling orientation customization of [33]. The reason for these specific methods is that one impacts domain size ratios, while the other retain periodic poling domain proportions.

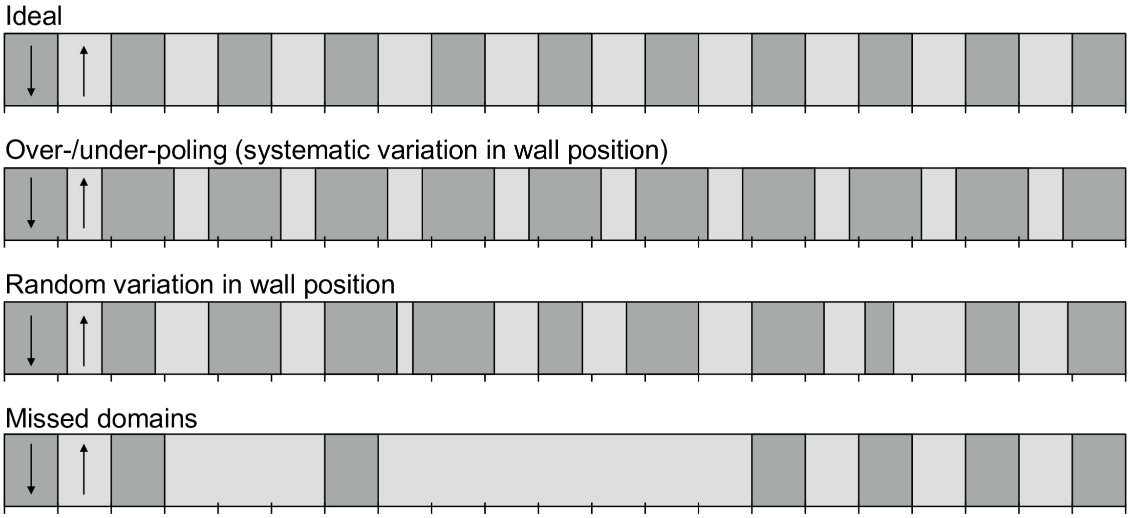

Figure 3.1: Schematic representation of the imperfections applied to the poling structure. Darker domains represent +1 orientation, and lighter ones the -1 sides [16].

3.2 Modelling customized poling structures

When modelling parametric down-conversion, a crystal is typically divided into N domains, to which a given poling orientation is assigned. This allows rewriting the integral inside of the PMF Equation (2.22) into a sum of N domain-sized integrals:

$$\Phi(\omega_i, \omega_s) = \sum_{j=0}^{N} s_j \int_{z_j}^{z_{j+1}} e^{i\Delta k(\omega_i,\omega_s)z} dz \,, \tag{3.1}$$

where z_j is the position where the jth domain starts and s_j is the poling orientation (± 1) for the jth domain. This equation format doesn't require uniform domains, so it can both be used to implement methods involving duty-cycle and poling customization. To do the simulations, a set of parameters for the Sellmeier's equation has to be given (see appendix A for more details), giving the Δk relation in Equation (3.1). Since KTP is one of the most common materials being used experimentally to generate single photons, it was used to probe the effects of imperfections on nonlinear shaping techniques.

Systematic changes in the arrays representing boundaries of Equation (3.1) were sufficient to model the first imperfection (overpoling/underpoling) entirely. Since it's an imperfection that deterministically influences the quality metrics of the process, only one simulation per percentage point is required to see the effect. Up to 5% deviation was found in [25], so we've checked the influence ranging from 0% to 15%, giving a broader range to allow more extreme cases to have data to refer to.

Missed domains were investigated by applying an algorithm to the poling structure that would flip poled domains randomly with a given probability. Since a given random simulation of impacted domains behave differently from another one, many simulations need to be ran in order to get a true representation of the impact of a given percentage of this imperfection.

In the case of the Gaussian noise on region positions, randomized fluctuations are added to domain walls. The process is mediated by a Gaussian distribution with, as its standard deviation, the percentage of variation that was selected. The algorithm was adapted to bypass the possibility of overlapping domains by having a strict boundary to previous/subsequent domain positions while iterating. In both cases, the analysis was performed on 100 generated data sets per % value, at which point the standard deviation on data would stop varying significantly by increasing the sets size.

Variations in dispersion we have studied were modelled by linear changes in Sellmeier's equation, as will be discussed in Section 3.3.4. This change of dispersion relation was chosen because different types of random variations were already addressed in [31]. We wanted to investigate how purity and amplitude change in a more deterministic variation of dispersion relation.

3.2.1 Physical conditions used in simulations

In most experiments, the bandwidth of the pump will be an intrinsically fixed parameter coming from the light source. Because of the fact that KTP achieve group-velocity matching (see Section 2.2.3) for a wavelength around $791.5nm$, the center of the pump was set at the corresponding frequency 2.38PHz, and given a bandwidth for the pump envelope function of $\sigma_{\text{PEF}} = 450\text{GHz}$. The degenerate photons of this conversion ($\omega_i = \omega_s = 1.16\text{PHz}$) lead to a coherence length of $23.05\mu m$, which is used as a domain size for both the periodic poling and customized domain orientation method.

The two poling methods studied generate a different PMF bandwidth for a given crystal length, which means that for a given pump width, the purity is impacted unless we adjust for this effect. This was taken in account by adjusting the length until the FWHM of the complementary photons spectral distribution (the diagonal $\bar{\omega}_p = \omega_s + \omega_i$ in the PMF) matched in the two curves. Customizing the domain orientation require an external algorithm dependant on the size of the crystal, therefore it was used as a benchmark with $N = 2000$ equally sized domains, giving a $L = 46.1mm$ sized crystal, which is also a realistic size for a waveguide. Customized duty-cycle had the best match when given $N = 1320$ domains, for a size of $L = 30.5mm$.

The discretization of the JSA and its spectral range can impose numerical artefacts when measuring the purity numerically [16]. In fact, when a spectral range is too narrow, the sidelobes responsible for diminishing the calculated purity can be outside of the selected window. For this reason, the spectral distributions was spread over a 100 by 100 grid, and a spectral range of $7.02THz$ was selected, at which point the purity would not significantly decrease by increasing the range.

Domain size was kept constant through the whole crystals for periodic and customized orientation poling, but since duty-cycle customization require a Gaussian progression of the duty-cycle, there has to be a minimal (and maximal) domain size for either orientation. This limit was set at $5\mu m$, as according to [10], the risk of missing domain poling below that value becomes too critical, giving an irregular poling.

3.3 Results

For every data point presented in this section, we compute the purity and amplitude of the JSA using a pump width optimized for a crystal with no imperfections. Amplitude is also normalized by dividing results by the amplitude of a periodically poled crystal of the same length.

3.3.1 Overpoling & Underpoling

Overpoling and underpoling were applied on the segment arrays by systematically increasing/decreasing the limits of a domain with a +1 orientation. Since the purity and amplitude also gets affected systematically, this allowed us to generate 75 data points over the $0\% - 15\%$ missed domain range and extracting the purity and amplitude of those points.

Since the duty-cycle starts at $10\% - 90\%$, subsequent +1 poled orientations would have their beginning and ends overlapping, so it's important to note that the code used to modify the domain size had a condition preventing this overlapping from happening by simply merging them into a full +1 domain (and vice-versa if the same effect is happening for the -1 domains).

In our model, underpoling is the inverse of overpoling. Since the crystal structure is symmetric from the center if the sign of all domains are flipped, it means that the two effects were effectively identical. Overpoling results also apply to underpoling.

Plots of the results of these simulations for overpoling, including all three methods' amplitude and purity progression for varying overpoling percentage values are shown on Figure 3.2. The data only show a marginal decrease for all three methods, and in both metric. This is surprising, as higher percentage points means that there is a good amount of domain-fusing happening in the duty-cycle method, but despite that, purity and amplitude remains within 1% of their initial values throughout. Another counter-intuitive result that we got is that when the simulations were pushed to the physical limit of domains sizes (100% overpoling), the amplitude didn't decrease linearly. In fact, it took a 50% overpoling value to reach a decrease of 25% in amplitude for periodic poling. This wasn't expected a priori; simply having half of the crystal periodically poled doesn't give the same result at all (in this case it would decrease by 50%), despite having the same area of inverted domains.

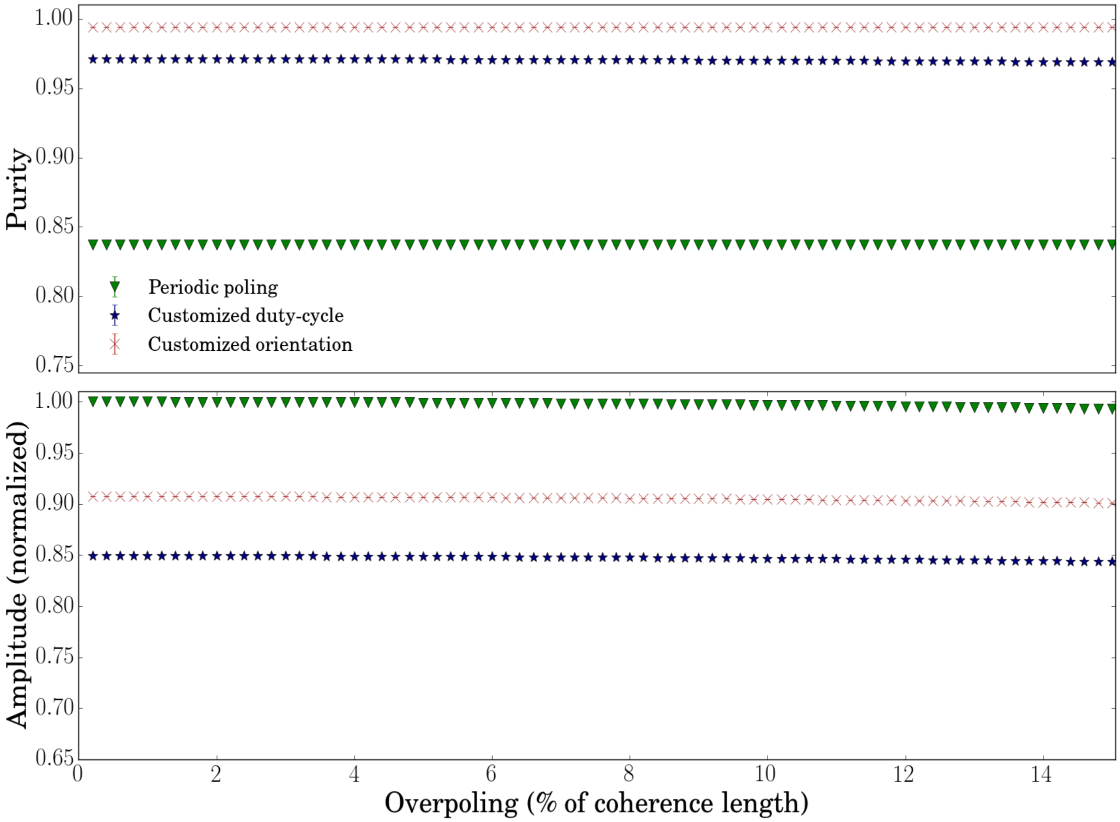

Figure 3.2: Amplitude and purity plotted as a function of the percentage of overpoling bias applied to domains, for three different poling methods.

3.3.2 Missed domains

Missed domains values were applied on the poling orientation arrays by stochastically altering the value of domains assigned to them. By using a Monte Carlo method to determine if, for a given probability of flipping, a $+1$ domain gets switched to a -1 one, we were able to simulate missed domains. However, in this case, one data point per percentage value is not sufficient as the order in which domains are flipped is random. For this reason, 100 simulations for each percentage value had their purity and amplitude averaged. A study of how the standard deviation was changing as a function of the number of simulated points lead us to this value, since it stopped significantly varying at around 80 points.

Results for these 100 simulations on the different methods are shown on Figure 3.3. In this case, amplitude decreased linearly, which was expected. As the percentage value increased, the amplitude gets increasingly spread around the average value, leading to more uncertainty in conversion efficiency. In the case of purity, however, there is almost no noticeable trend in either the progression of purity itself or the spread of its value, aside from periodic poling. This clearly indicates that customized nonlinearity profiles from either customized duty-cycle or orientations are very robust against missed domains imperfections in their role of generating pure single photons.

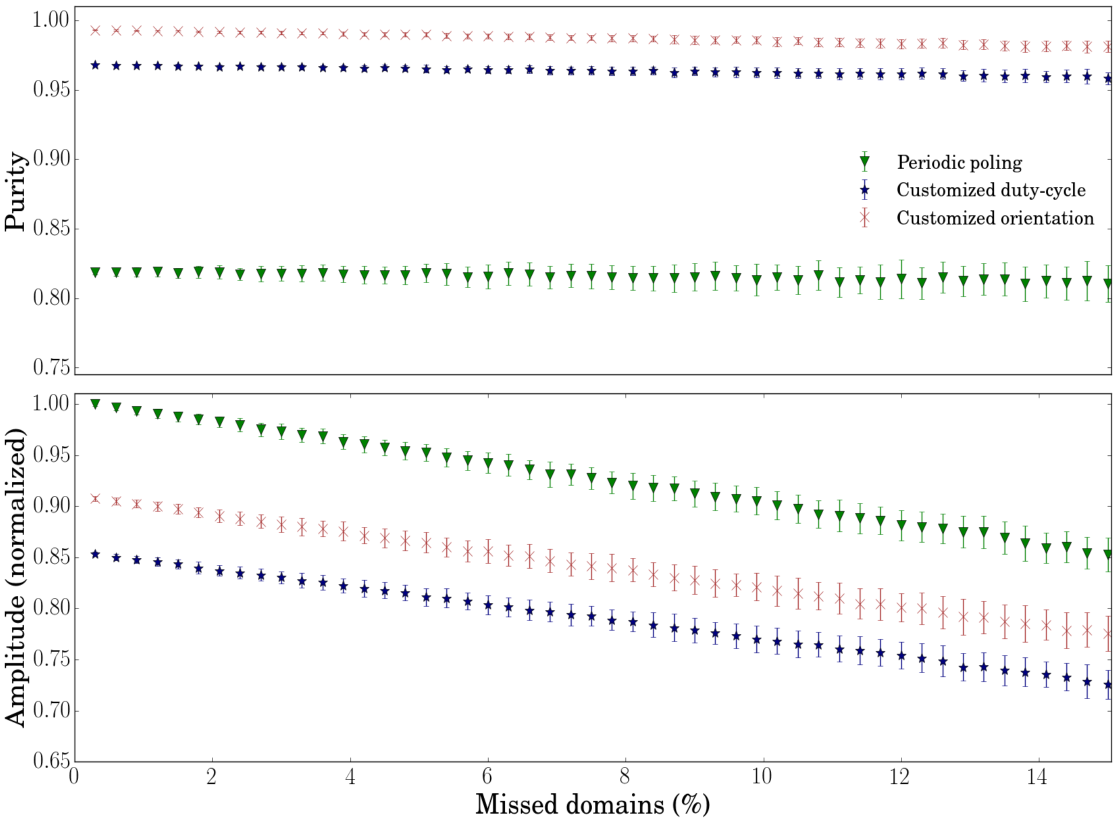

Figure 3.3: Amplitude and purity plotted as a function of the percentage of missed domain flips along the crystal, for three different poling methods.

3.3.3 Randomized Variations in Wall Positions

Variation on domain wall positions were also added using a randomized method. Monte Carlo simulations of a Gaussian distribution around each domain positions added a randomized value to their start and end points. The standard deviation of the Gaussian distribution was set to match a percentage of the coherence length of the crystal. Similarly to the overpoling imperfection, boundaries had to be set to ensure that domain overlap does not happen. Also, as in the missed domain imperfection, 100 data points per percentage had to be collected to ensure an accurate representation of results. Values up to 12% of the coherence length were used, as experiments reported up to a value of 8% for lithium niobate crystals ([29],[28])

For this imperfection, results show a strong stability to variation, with a similar curve for purity as in the two previous cases, as the results show on Figure 3.4. As we can see, amplitude decrease only starts happening for higher values of deviations, but maintain a lower standard deviation than in the missed domain case, indicating an higher stability to imperfections.

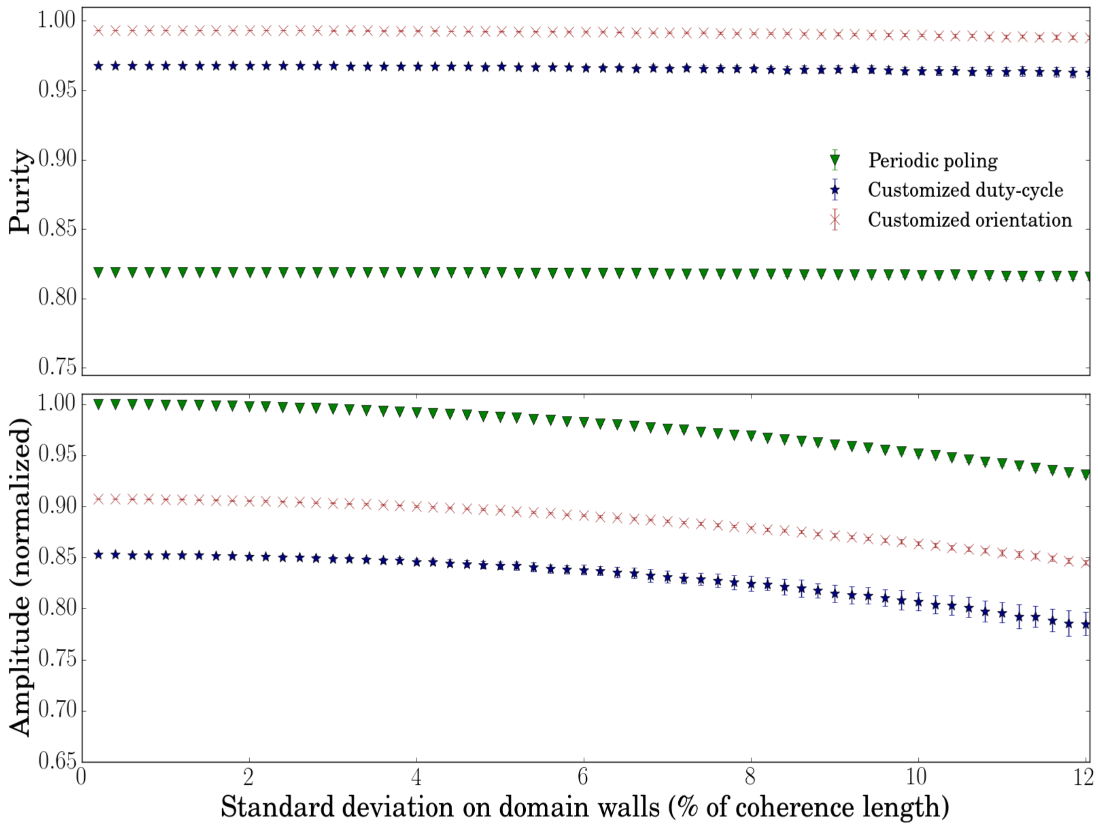

Figure 3.4: Amplitude and purity as a function of the standard deviation (%) of variation on domain position, for three different poling methods.

3.3.4 Variations in dispersion relations of materials

By modifying Sellmeier's parameters (see Appendix A) using a linear, position dependant function, we were able to modify the dispersion relations in the crystal. A linear change of Sellmeier's parameter lead to a linear change in dispersion equations. Figure 3.5 illustrates how a 20% change in all of Sellmeier's parameter, spread uniformly around the center of the crystal, impacts the dispersion relations for degenerate photons generated from the central frequency of the pump. As we can see, the refractive index fluctuates by about 20% over the range of the crystal. This allows us to simulate a linear variation in dispersion relations.

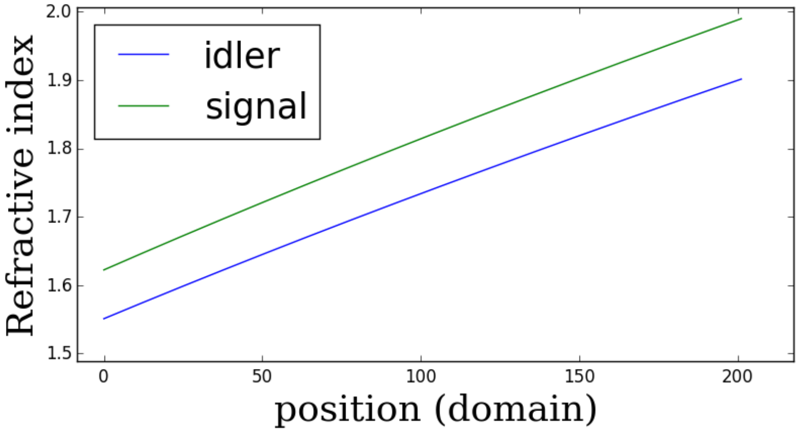

Figure 3.5: Refractive index at the degenerate, central frequency, for the two axis in a crystal with a 20% variation in Sellmeier's equation over its length.

We have applied up to a 20% variation in the dispersion relations, equally distributed around $\frac{L}{2}$ and studied its effect on the two domain engineering methods. It's important to note that the calculations involving the PMF were using Equation (4.3), which correctly takes in account dispersion relations (more about this in Section 4.3). Figure 3.6 show the results of the simulations. As we can see, variations in dispersion relation impact purity and amplitude significantly for both methods.

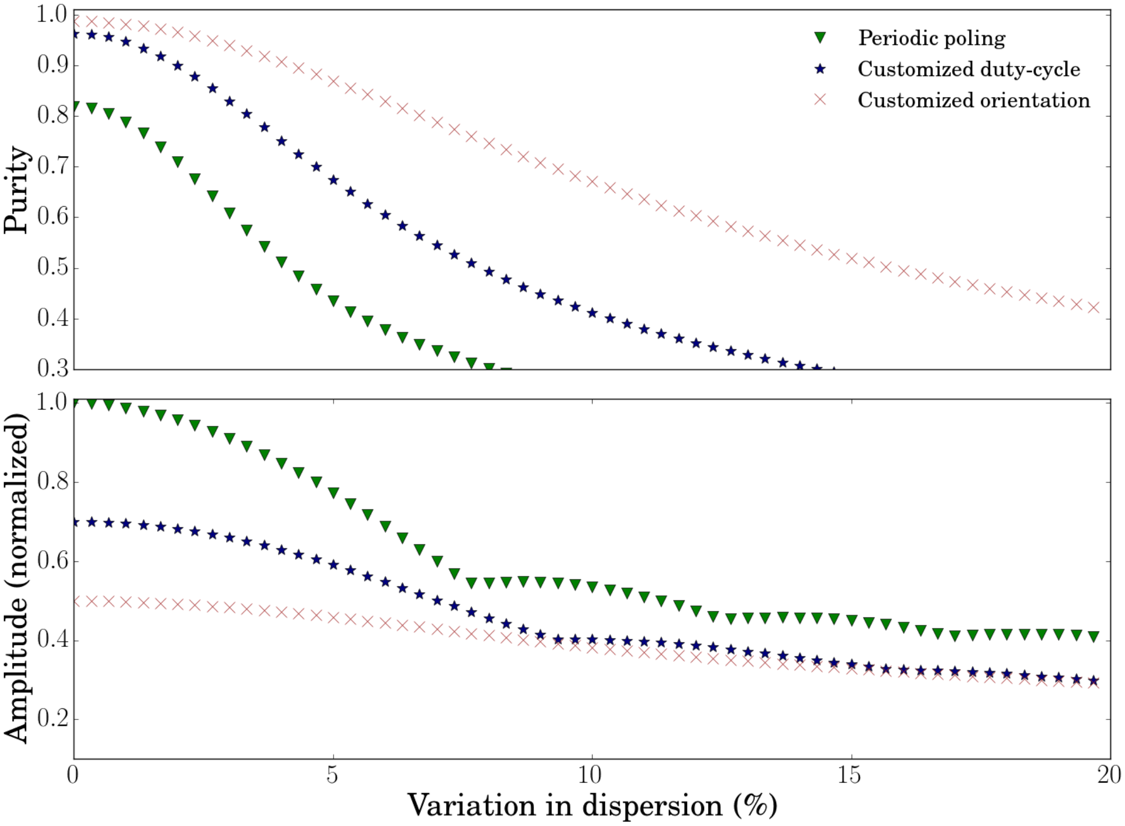

Figure 3.6: Amplitude and purity plotted as a function of the percentage of variation in the dispersion relation along the crystal, for three different poling methods.

3.4 Conclusion

Overall, for the three first imperfections analyzed (i.e overpoling, missed domains and randomized duty-cycle), it is clear that the imperfections in crafting the crystals have little impact in the purity. This is of significant importance as it means that using a customized nonlinearity to achieve a Gaussian phasematching is an highly predictable tool, especially considering that experiments have reached as high as $92.9 \pm 1.6\%$ purity without the use of filtering, using the customized duty-cycle method [6]. Nonetheless, it would be good to pursue this research in the case where noise on domain walls is correlated. Numerical simulations have shown that correlated variations of dispersion relations can impact the purity significantly [31].

For the last imperfection studied, results show a strong relationship between variations of dispersion and loss of purity and efficiency. If materials with changes in their refractive index are used in the design of experiments involving the generation of pure single photons, additional engineering will be required. Fortunately, this can be done as we will see in the next chapter.

3.5 Notes and acknowledgments

The results from this section were published in:

Francesco Graffitti, Jérémy Kelly-Massicotte, Alessandro Fedrizzi, and Agata M Brańczyk. Design considerations for high-purity heralded single-photon sources. Physical Review A , 98(5):053811, 2018.

The paper was co-written by all authors, but the simulations and analysis presented in this chapter are the work of Jérémy Kelly-Massicotte.

Chapter 4

Pulse shaping in medium with longitudinally varying dispersion relations

4.1 Motivation

As was shown in Section 3.3.4, the current state of domain engineering to generate pure single photon generation is inapplicable to materials that have varying dispersion relations. Correlated noise variations are known to impact the fabrication of Ti:LN waveguides [31], as a change in the geometry of a waveguide can change its dispersion relation, conducing to a loss of the conversion features of the waveguide. It's possible that a clever domain engineering design could function as a countermeasure to this problem.

On another note, variations in the dispersion could be an intentional feature in future experiments, where a change of material or geometry could be required. For example, in adiabatic tapers, the geometry of a waveguide is slowly varied in order to funnel light and ensure that the optical modes are not changing. Tapers are usually regions where domain engineering is not efficient, as changes in dispersion leads to low purity. This is why developing the right tools for optimal purity and conversion in medium with varying dispersion is paramount.

In this chapter, we show how we can manipulate the PMF shape of PDC photon pairs in a material with changing dispersion. We present the analytical derivation of a target function used to reach a Gaussian PMF, numerical simulations applying it, and introduce a different method which uses variation in domain size to reach high purity.

4.2 Customized poling algorithm

Customized poling techniques can improve the purity of single photons in $\chi^{(2)}$ nonlinear materials. Not only do they allow the photons to have a PMF that is Gaussian, hence having the optimal shape for separability [30], but they allow customization of the width of this Gaussian. While an early method from [11] allowed a stochastic solution using simulated annealing to generate a poling structure, recent deterministic methods have since superseded it. Two deterministic customized poling orientation methods have emerged in the last few years', with [33] giving a fully customized poling structure for equally sized domains, and [18] aimed at allowing sub-coherence length domains for the customization. In this section, we will cover how a deterministic customized poling orientation algorithm work.

We've seen previously, in Section 2.3.3, that taking the Fourier transform (FT) of a PMF leads to the $g(z)$ function, which tells us how the poling orientations are distributed in the crystal. This is given by the following equation:

$$g(z) = \int_{-\infty}^{\infty} \phi(\Delta k) e^{-i\Delta k z} d(\Delta k). \tag{4.1}$$

However, Equation (4.1) is a continuous, complex function. Therefore it's not possible to use this $g(z)$ as a guide to electrically pole a crystal, since the only physically possible options are $+1$ or -1 orientations. Fortunately, there is a one-to-one mapping between the way the amplitude for a Δk value grows as a function of position for a given resulting PMF. Customized poling methods from [33] and [18] make use of this fact in creating nonlinearity profiles that can be implemented. Figure 4.1 shows how the progression of the amplitude of periodic poling and customized poling generated from the method in [33] differs. As we can see, a Gaussian PMF has an amplitude that has a progression reminiscent of an error function, while the periodic poling has a linear progression.

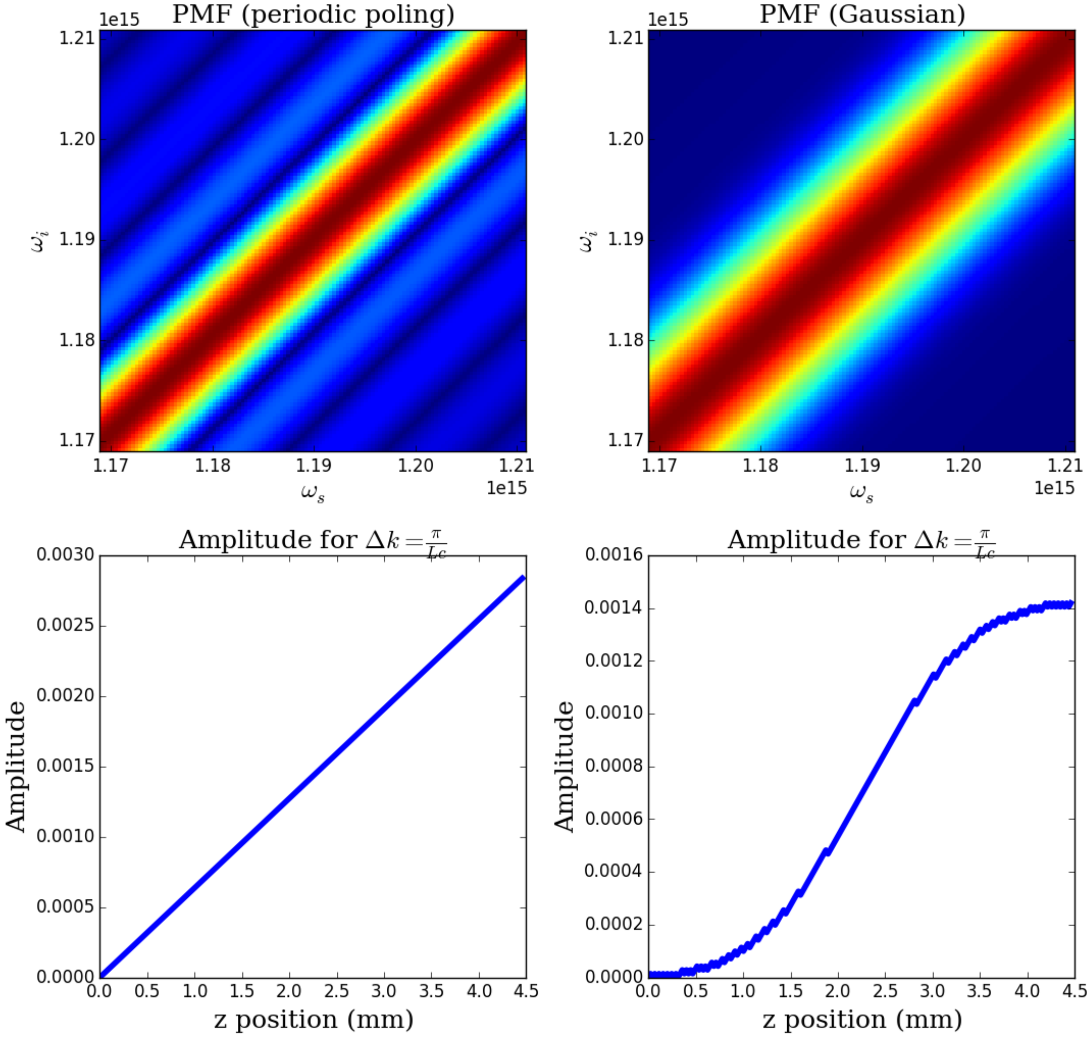

Figure 4.1: Illustration of how the amplitude function for degenerate photons progress for two PMF's generated by different poling methods.

This can subsequently be used in a numerical algorithm constructing a crystal, piece by piece, by matching the amplitude of the degenerate photons for the PMF structure that is wanted. The algorithm follows this structure:

1. Specify a target function $\phi(\Delta k)$, and Fourier transform it into a $g(z)$ using Equation (4.1). This $\phi(\Delta k)$ will typically be a Gaussian function if the purpose is to generate pure single photons.

2. Calculate the PMF at the central phasematching value Δk_0, where degenerate photon pairs comes from the central frequency of the pump. This is done by taking the integral of Equation (2.26) for a position z inside of the crystal:

   $$\phi(\Delta k_0, z) = \int_0^z e^{i\Delta k_0 z'} g(z') dz', \tag{4.2}$$

   with the $g(z')$ coming from the Fourier transform of Step 1. This function is referred to as the target function.

3. Build a poling structure by using a cost-function which discriminate the optimal choice between picking $+1$ and -1 values for an upcoming domain. By iterating through every domains in the crystal, the cost-function compares the amplitude changes for both orientations choices and select the one which has the least distance from the target function. In other words, it calculates Equation 4.2 for a given z, and attempt to follow the direction of the amplitude at $z + \Delta z$ of the target function.

Once this is done, the poling structure can be applied to a nonlinear crystal, and the outcome will give a photon pair PMF which, to a good approximation, matches the target PMF.

4.3 Customized poling algorithm on crystals with varying dispersion relations

As we saw in Section 3.3.4, changes in dispersion reduces the purity. In this section, we will attempt to compensate for this by modifying the algorithm presented in the previous section to take variable dispersion into account. This will require a redefinition of the PMF equation and the derivation of an alternative expression for the target function.

Modifying the algorithm to account for variable dispersion is not trivial. This is because taking the Fourier transform of Equation (4.1) no longer describes the $g(z)$. This is caused by the fact that the changing dispersion imply a z dependency in the phase mismatch (Δk). Additionally, calculating the phasematching function has to be done differently; taking a sum over individual domains, as is done in Equation (3.1), is invalidated because the change of dispersion leads to an incorrect starting phase when summing domain contributions to the PMF. The equation taking in account this phase correction is shown on Equation (4.3). Adding an integral over the position dependant phase mismatch in the complex phase exponential of Equation (2.26), we can correctly take in account the changes in dispersion.

$$\phi(\omega_s, \omega_i) = \int_0^L g(z) e^{i \int_0^z \Delta k(z') dz'} dz. \tag{4.3}$$

We are not aware of any formal proof of Equation (4.3) in literature despite its presence in previous literature (e.g [21]). For this reason, appendix B contains the derivation of a method to compute the PMF taking in account the dispersion change, by summing contributions of domains with a correct phase. This method was shown to give the exact same results as Equation (4.3) using numerical simulations of both equations. Since the Appendix's equation is slightly less practical, we have used Equation (4.3) for our simulations and analytical derivations.

In this section, we will show how to apply the previous section's method to a crystal with an arbitrary monotonic z-dependant dispersion. A different definition of $\Delta k(z)$ will allow the derivation of an alternative target function to use in step 1 and 2 of the method from Section 4.2.

4.3.1 Definitions

To first order, phase mismatch can be written as

$$\Delta k(\omega_i, \omega_s) = k_{i,0} + k_{s,0} - k_{p,0} + k'_i(\omega_i - \bar{\omega}) + k'_s(\omega_s - \bar{\omega}) - k'_p(\omega_i + \omega_s - 2\bar{\omega}) \tag{4.4}$$

with $\bar{\omega}$ being the central degenerate frequency of the process, that is half of the pump central frequency, and k'_x representing the derivative $k(\omega_x)$ with respect to ω_x, evaluated at its respective central frequency. A first order expansion is sufficient, as the pump spectral distribution is typically small compared to its central frequency. The spectrum of the PMF that intersects it is incidentally located really close to the central frequencies of the degenerate photons, justifying the first order expansion.

It's important to note that there is an implicit z and ω_x dependency on every k_x terms in Equation (4.4). Under symmetric group velocity matching conditions $k'_p = \frac{k'_1+k'_2}{2}$, which means that by using three substitutions:

$$a(z) = k_{i,0} + k_{s,0} - k_{p,0} - (k'_i + k'_s - 2k'_p)\bar{\omega} - \bar{\omega}(k'_i - k'_s), \tag{4.5}$$

$$b(z) = c(k'_i - k'_s), \tag{4.6}$$

and

$$\kappa = \frac{\omega_i}{c} = \frac{2\bar{\omega} - \omega_s}{c}, \tag{4.7}$$

we can rewrite Equation (4.4) as

$$\Delta k(\omega_i, \omega_s) = a(z) + b(z)\kappa, \tag{4.8}$$

to distinguish a frequency dependant $(b(z)\kappa)$, and frequency independent $(a(z))$ component to the phase mismatch. Equation (4.5) is valid since we are looking exclusively at the complimentary photons $(\omega_i + \omega_s = 2\bar{\omega})$ of the distribution. We can also define

$$\tilde{a}(z) = \int_0^z a(z')dz', \tag{4.9}$$

and

$$\tilde{b}(z) = \int_0^z b(z')dz'. \tag{4.10}$$

With these definitions, we can rewrite Equation (4.3) as:

$$\phi_{target}(\kappa) \equiv \phi(\kappa) = \int_0^L g(z) e^{i(\tilde{a}(z)+\tilde{b}(z)\kappa)} dz, \tag{4.11}$$

in which κ becomes the only term with a frequency dependency. We define this as the target PMF $\phi_{target}(\kappa)$, and it represents the phasematching function of complimentary photons in a crystal of length L, with poling profile $g(z)$. The advantage of that expression is that the exponential in the integral has an separate frequency dependency, which will allow it to be manipulated more easily. Now, the integral in Equation (4.11) is bounded from 0 to L because it is assumed that the crystal has a finite length, and so the $g(z)$ expression is 0 outside of the integral's range. In general, this is not the case, and we can write a general PMF equation where no assumption is made about limits:

$$\Phi(\kappa) = \int_{-\infty}^{\infty} g(z) e^{i(\tilde{a}(z)+\tilde{b}(z)\kappa)} dz. \tag{4.12}$$

We also need to define a function that will be used in the customized orientation algorithm, following a similar cost-function approach as presented in Section 4.2. It will serve as the goal amplitude for degenerate photons, which will allow the creation of a poling structure generating a PMF behaving like the target function $\phi_{target}(\kappa)$ at $z = L$. Such a function can be written as

$$\Phi(\kappa_0, z) = \int_0^z g(z') e^{i(\tilde{a}(z')+\tilde{b}(z')\kappa_0)} dz'. \tag{4.13}$$

4.3.2 Derivation of an expression for the amplitude growth

To be able to effectively model a target amplitude to use in the cost function of the customized orientation method presented in Section 4.2, we need to Fourier transform Equation (4.11) to get the corresponding $g(z)$, then put the result back into Equation (4.12) for degenerate photons ($\kappa = \frac{\bar{\omega}}{c}$) to compute the target amplitude for different values of z (Equation (4.13)).

By taking the Fourier transform of Equation (4.12), we get that

$$\int_{-\infty}^{\infty} d\kappa \Phi(\kappa) e^{-i\kappa z'} = \int_{-\infty}^{\infty} dz g(z) e^{i\tilde{a}(z)} \int_{-\infty}^{\infty} d\kappa e^{i\tilde{b}(z)\kappa} e^{-i\kappa z'}. \tag{4.14}$$

As we can see, the rightmost integral of Equation (4.14) leads to a delta function. We can rewrite it as

$$\int_{-\infty}^{\infty} d\kappa \Phi(\kappa) e^{-i\kappa z'} = \int_{-\infty}^{\infty} dz g(z) e^{i\tilde{a}(z)} (2\pi\delta(\tilde{b}(z) - z')). \tag{4.15}$$

Now it's not simple to extract the value of z for which $\tilde{b}(z)$ is equal to z'. However, as long as $\tilde{b}(z)$ has a monotonic mapping to its inverse, we can replace z by the inverse $\tilde{b}(z)$ function of another variable, z''. In other words we can substitute $\tilde{b}^{-1}(z) = z''$ and $z = \tilde{b}^{-1}(z'')$ in Equation (4.19) to get:

$$\int_{-\infty}^{\infty} d\kappa \Phi(\kappa) e^{-i\kappa z'} = 2\pi \int_{-\infty}^{\infty} d(\tilde{b}^{-1}(z'')) e^{i\tilde{a}(\tilde{b}^{-1}(z''))} g(\tilde{b}^{-1}(z''))\delta(z'' - z'). \tag{4.16}$$

By expressing the differential of the inverse function of $\tilde{b(z)}$ as a total derivative, with z'' as the only variable:

$$d(\tilde{b}^{-1}(z'')) = dz''(\frac{d(\tilde{b}^{-1}(z''))}{dz''}), \tag{4.17}$$

hence giving the integral of the right hand side of Equation (4.16) a simple expression. If we substitute it back in it, we get

$$2\pi \int_{-\infty}^{\infty} dz''(\frac{d(\tilde{b}^{-1}(z''))}{dz''}) e^{i\tilde{a}(\tilde{b}^{-1}(z''))} g(\tilde{b}^{-1}(z''))\delta(z'' - z') = 2\pi(\frac{d(\tilde{b}^{-1}(z'))}{dz'}) e^{i\tilde{a}(\tilde{b}^{-1}(z'))} g(\tilde{b}^{-1}(z')) \tag{4.18}$$

Since z" is an arbitrary variable, we can substitute back the inverse function to $z' = \tilde{b}(z)$ and $\tilde{b}^{-1}(z') = z$ in Equation (4.14), with the right side of Equation (4.18) to get:

$$\int_{-\infty}^{\infty} d\kappa \Phi(\kappa) e^{-i\kappa\tilde{b}(z)} = 2\pi(\frac{dz}{d(\tilde{b}(z))})e^{i\tilde{a}(z)}g(z). \tag{4.19}$$

We can see that the derivative on the right is the reciprocal of the derivative of Equation (4.10), so we can rewrite

$$\int_{-\infty}^{\infty} d\kappa \Phi(\kappa) e^{-i\kappa\tilde{b}(z)} = \frac{2\pi e^{i\tilde{a}(z)}}{b(z)}g(z). \tag{4.20}$$

If we assume that the $g(z)$ function is 0 everywhere except inside of a crystal, we can see that Equation (4.11) and Equation (4.12) are the same. Since we want to study the cases where interaction only happens inside nonlinear material, then we can write $\Phi(\kappa) = \phi_{target}(\kappa)$. By doing so and isolating $g(z)$, we get:

$$\frac{e^{-i\tilde{a}(z)}b(z)}{2\pi}\int_{-\infty}^{\infty} d\kappa \phi_{target}(\kappa) e^{-i\kappa\tilde{b}(z)} = g(z). \tag{4.21}$$

Equation (4.21) gives us a continuous description of how the nonlinearity factor has to change, while restricted from 0 to L in z, to get the target function $\phi_{target}(\kappa)$. This is not sufficient however, as poling only allow discrete $+1$ or -1 values for $g(z)$. This means that we need to convert this $g(z)$ to a target amplitude growth to use in the customized poling algorithm. To do so, we substitute back the expression for $g(z)$ in Equation (4.21) into Equation (4.13), to get :

$$\Phi(\kappa_0, z) = \int_{-\infty}^{\infty} d\kappa \phi_{target}(\kappa) \int_{0}^{z} \frac{b(z')}{2\pi} e^{i\tilde{b}(z')(\kappa_0-\kappa)} dz'. \tag{4.22}$$

4.4 Implementation of the modified algorithm

We have done simulations following the steps of Section 4.2, by replacing the step 2 Equation 4.2 by Equation (4.13). The crystal length used in simulations was $4.46mm$, containing approximately 200 domains. The reason for using a small crystal was to spare computing time, as the process of recreating the poling structure require a calculation of the PMF twice for every iteration, and the time of calculation is proportional to the size of the crystal. A method to optimize the pump width was implemented in the algorithm to ensure that the purity of the JSA is maximal with every PMF shape that we output. Optimization was based on a $\sigma_{\mathrm{PEF}} = 3.07$THz pump envelope function standard deviation. Standard KTP Sellmeier's equations were used as the basis for dispersion relations, and accordingly, a central pump wavelength of 791.5nm, at which KTP is group-velocity matched for PDC. Length of the two-dimensional grid holding the double frequency dependence was set to 120 by 120 to ensure the least numerical errors as possible.

4.4.1 Linear change in dispersion

The algorithm was applied to various linear change percentages, ranging from 0 to 90%. Figure 4.2 shows the resulting purity and maximal PMF amplitude extracted from the resulting poling structures.

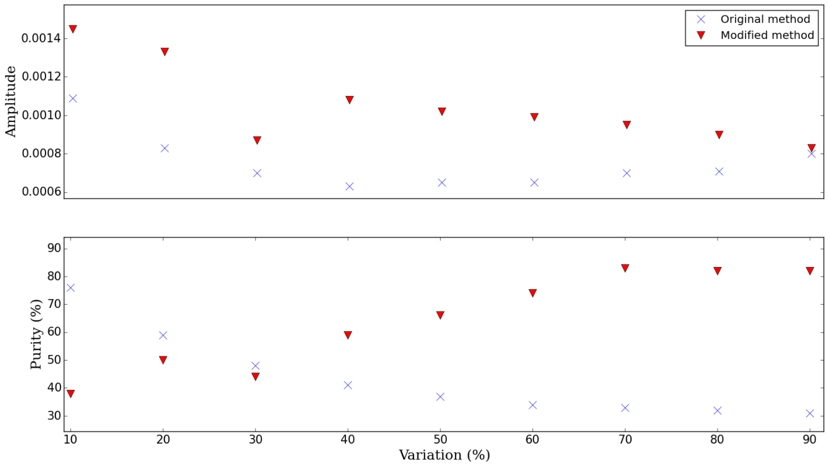

Figure 4.2: Maximal amplitude and purity of the PMF for different variations of the refractive index spread through the crystal length. The regular method for generating Gaussian PMF (original method) is compared with our modified poling method (modified method).

We refer to as “original method“ the poling structure obtained from [33], which would generate a Gaussian PMF in materials with no dispersion changes. As shown, the amplitude becomes worse as the variation gets bigger in both cases. However, the purity increases for our algorithm and the purity of the original method poling structure decreases. At values of 30% variations in dispersion relations, we can see that our algorithm starts performing significantly better, reaching purity values of about 80% for extreme dispersion variations. We are unsure at this point in time why our algorithm performs worse for lower variations, but we think it could be related to the fact that static domain sizes were used in the algorithm.

An example of the PMF (top) and JSA (bottom) that were extracted from applying the regular customized poling method without correcting the target function (original method) and the modified one (modified method) are shown on Figure 4.3, for two different variation percentages. As we can see, the modified method improves the amplitude and purity.

On Figure 4.3 a), a 10% variation on dispersion relations is shown and in Figure 4.3 b), a 50% variation. As we can see from the picture, the side lobes of the corrected poling attenuate at the higher percentage value, which seems to explain why the purity is better than in the 10% case. We can also see that the regular customized poling method doesn’t conserve its shape when dispersion changes, which is why it decrease significantly in both amplitude and purity.

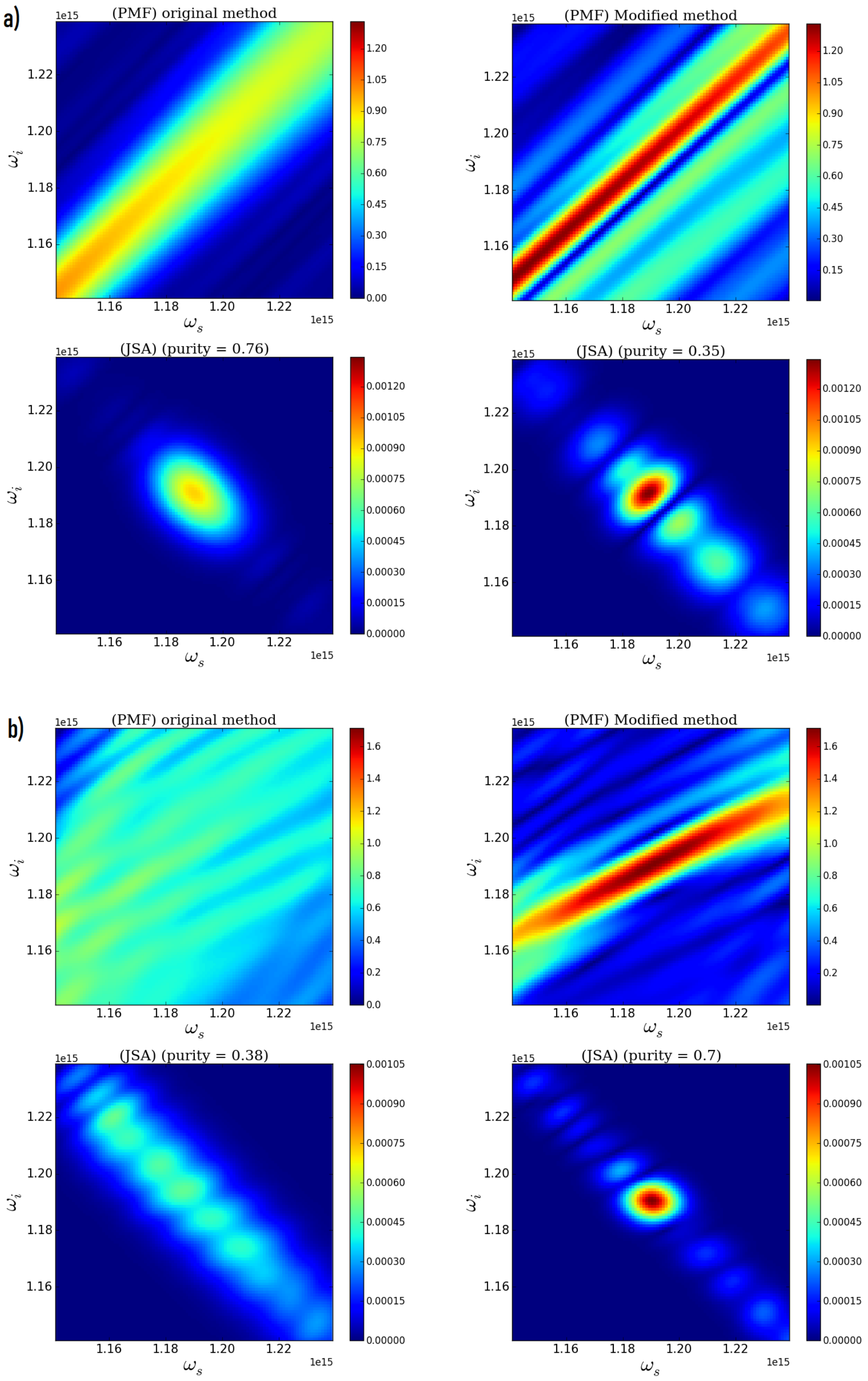

Figure 4.3: Example of the PMF and JSA obtained from a 46mm crystal affected by a linear change in its dispersion relations, for customized poling using a modified algorithm (modified method) and for a non-optimal solution from the original method (original method). a) 10% change in dispersion. b) 50% change in dispersion.

4.4.2 Discussion of results

As we saw in this section, the algorithm only poorly reproduces a Gaussian phasematching function. We believe this is caused by the fact that each subsequent domain don't coherently add to the phase of the previous ones, so there is a limit to how good the algorithm can match the amplitude growth using poling. Figure 4.4 shows how the amplitude growth compare with the target function for a 50% linear variation in dispersion relations. As we can see, large deviations from the optimal path happens. In fact, deviations are so strong that the output of the algorithm trying to optimize purity performs worse in maximizing purity than a customized poling optimized for constant dispersion, if the variation is modest.

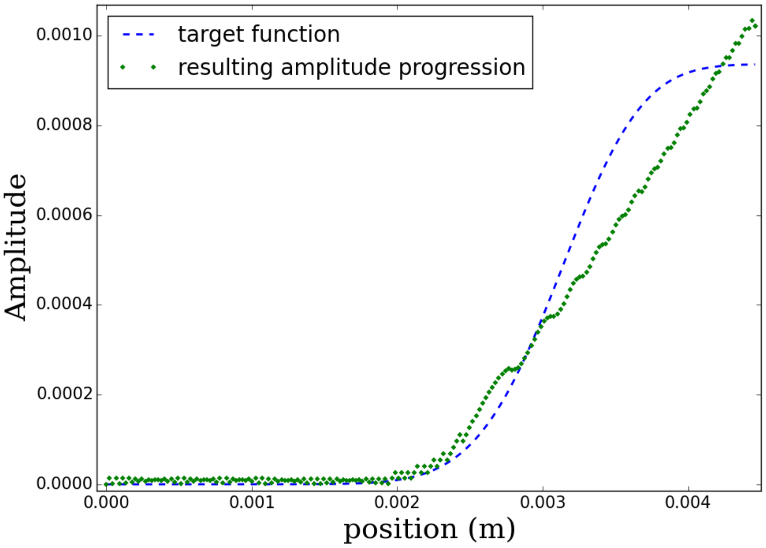

Figure 4.4: Comparison between the expected amplitude growth (target function) and the algorithm produced amplitude growth (resulting amplitude progression) through a 46mm crystal with a linear 50% variation in dispersion.

4.5 Adapting domains to phase mismatch

The second approach we have found to generate a Gaussian PMF for crystal with varying dispersion involves varying the domain sizes. By creating a crystal whose domains change by matching the coherence length $L_c = \pi/\Delta k(\bar{\omega})$ associated with the phase mismatch $(\Delta k(\omega))$ of the domains (see Figure 4.5), destructive interference caused by the change of starting phase that happens in a structure with varying dispersion and constant domain size disappears. This means that the amplitude for degenerate PDC photons coming from the central frequency of the pump grows in the same way as they would in a structure with constant dispersion. This means that in order to optimize the central degenerate frequency conversion efficiency, periodic poling remain the optimal solution.

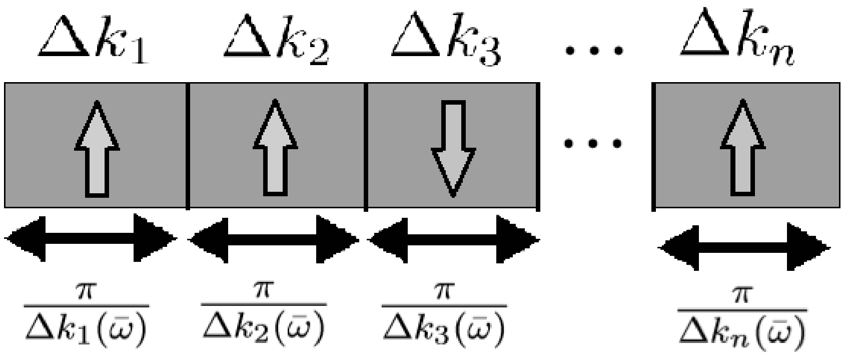

Figure 4.5: Illustration of a method to get a Gaussian phasematching function in a crystal with varying dispersion.

What's harder to predict is how the rest of the PMF behave to an adapting change in the length of domains. It turns out that a customized poling structure generated for a crystal with no variation in its dispersion applied to a varying dispersion crystal with adjusted domain lengths almost entirely retains its JSA shape, even for extreme cases. Figure 4.6 compares the JSA and PMF of a 0% and 50% variation in dispersion applying the domain size adjustments, and keeping the customized poling orientation structure given by [33]. We can see that the PMF loses its shape when getting further away from the top-right to bottom-left diagonal, however, for our purposes, this is the important part of the PMF, as this is where the pump envelope function intersects it to form the JSA. This is why the purity remains near-unity despite having an altered PMF.

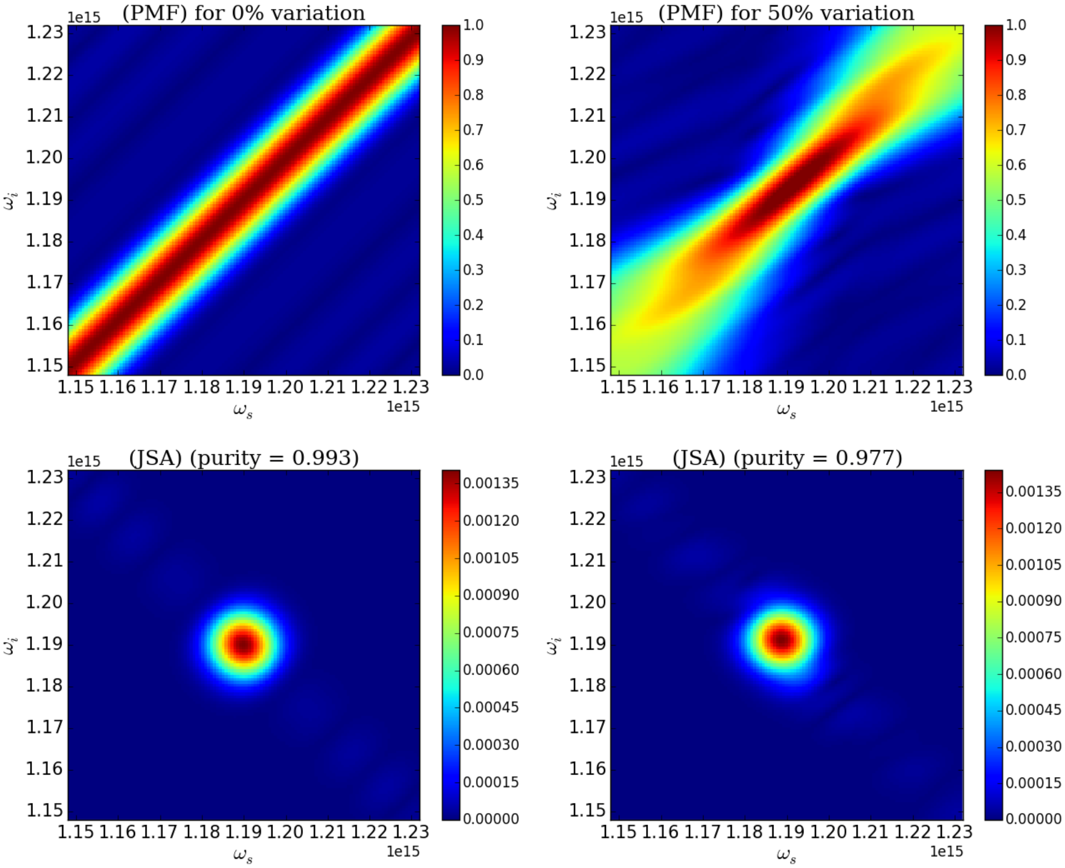

Figure 4.6: PMF and JSA obtained from a 46mm crystal affected by a linear change in its dispersion relations, adjusting domain size to coherence length, for 0% and 50% changes in dispersion.

A similar analysis as the one performed in Section 4.4.1 is shown on Figure 4.7. As we can see from the corrected domains curve, there is almost no decrease in purity coming from the variation in dispersion. This shows that adjusting the domain width to match the coherence length is an effective method to increasing the purity of single photons in a varying dispersion material.

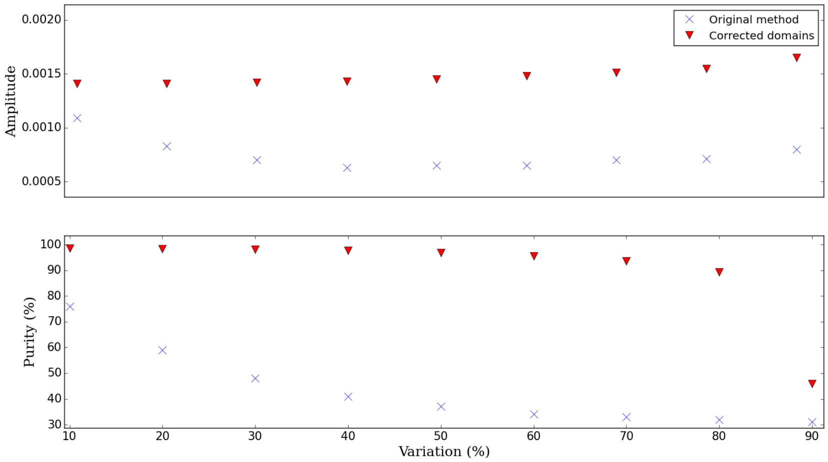

Figure 4.7: Maximal amplitude and purity of the PMF for different variations of the refractive index spread through the crystal length. The original method to get Gaussian PMF (original method) is compared with the corrected domains method (corrected domains).

4.6 Conclusion

As we could see from the results presented in this chapter, achieving high purity for single photons in materials with variations of dispersion was made possible with two different methods that we proposed.

In the first one, poling orientations were customized in a structure with constant domain sizes, and lead to a growing purity as the variation was increased. However, this method performed modestly at low variations. This could possibly be improved by taking a cost-function making use of more than one point in the amplitude function.

In the second method, we have adapted the domain sizes to match the coherence length associated with the phase mismatch given by the local dispersion relations. Purity and maximal amplitude obtained by this method was almost identical to what is obtained in a structure with no changes in dispersion. Nevertheless, it would still be interesting to see if it could be improved by a stochastic method such as simulated annealing [12].

The domain variation method is a strong candidate for domain engineering to achieve a Gaussian PMF in medium with varying dispersion relations. Furthermore, the customized poling orientation method generated a PMF which had a more robust shape away from degenerate photon frequencies, which could be useful when PMF shaping is the focus of an experiment.

4.7 Note and acknowledgments

Results presented in this section are not published, but the credit for the research presented in it is divided in the following way:

1. Derivation of an analytical expression for the target function (Section 4.3) : **Agata M Brańczyk**, **Matteo Santandrea**, **Jérémy Kelly-Massicotte**.
2. Numerical simulations and analysis of results (Section 4.4): **Jérémy Kelly-Massicotte**
3. Domain size variation method (Section 4.5) : **Jérémy Kelly-Massicotte**

Chapter 5

Conclusion

The efficient generation of high-purity single photons is one of the most important goals of quantum optics. In this thesis, we have focused on the generation of single photons with high spectral purity using heralded parametric downconversion. In particular, we considered domain-engineering methods, which can be used to bring the spectral purity very close to unity. The main contributions of this thesis are: 1) the analysis of the effects of fabrications imperfections in domain-engineering on spectral purity and photon-pair amplitude (which is related to photon generation efficiency), and 2) introduction of two new custom poling approaches that take into account variations in dispersion within the waveguide.

In Chapter 3, we have characterized the purity and amplitude of two domain engineering methods affected by fabrication imperfections. By using numerical simulations, we have shown that structures impacted by overpoling, domain missing and randomized variations in wall positions in a realistic amount had only a marginal difference in purity and amplitude to ideal structures. We have also explored linear variations in dispersion relations, and saw that strong changes of refractive index lead to a loss of purity and amplitude. As long as the fabrications imperfections are kept at a realistic level, our results have shown that the domain engineering method are robust, predictable tools for generating pure single photons. It would be good to further explore other possible fabrication imperfections which were not tested for on the domain engineering methods. For example, a recent experiment showed that correlated noise in the dispersion relation could be impacting the fabrication of waveguides [31], which could be an interesting thing to explore in domain wall positioning.

In Chapter 4, we have presented two domain engineering methods adapted for medium with varying dispersion relations. In the first method, we proposed the rework of a deterministic customized poling orientation method from [33], using a different expression to take in account dispersion changes. This method had increasing effectiveness as the dispersion was increased, but had modest results cases of low variations. In the second method we proposed, domain size were varied in order to keep the quasi-phasematching conditions for the local dispersion relations. Coupled with a customized poling structure, this second method gave very high purity and amplitudes, even in the extent of very high changes in dispersion relations. With this method we have shown that generating high purity single photons in medium with varying dispersion relations is possible. In the future, it would be interesting to take in account more than one point in the cost function recreating the position dependant amplitude of our method. This could allow a more rigorous fidelity to the targeted phasematching function shape. Additionally, it would be interesting to see how stochastic methods, such as simulated annealing [12], could improve both methods results.

The fabrication imperfections simulations results we have presented will give confidence to future experiments involving the generation of single photon through parametric downconversion. Additionally, having the possibility to generate pure photons even in a medium with varying dispersion might enhance the capabilities of compensating for structural changes in waveguides, or even open possibilities to other innovative applications.

References

[1] Charles H Bennett and Gilles Brassard. Quantum cryptography: public key distribution and coin tossing. *Theor. Comput. Sci.*, 560(12):7–11, 2014.

[2] Dik Bouwmeester, Jian-Wei Pan, Klaus Mattle, Manfred Eibl, Harald Weinfurter, and Anton Zeilinger. Experimental quantum teleportation. *Nature*, 390(6660):575, 1997.

[3] Robert W Boyd. *Nonlinear optics*. Elsevier, 2003.

[4] Agata M Brańczyk, Alessandro Fedrizzi, Thomas M Stace, Tim C Ralph, and Andrew G White. Engineered optical nonlinearity for quantum light sources. *Optics express*, 19(1):55–65, 2011.

[5] Changchen Chen, Cao Bo, Murphy Yuezhen Niu, Feihu Xu, Zheshen Zhang, Jeffrey H. Shapiro, and Franco N. C. Wong. Efficient generation and characterization of spectrally factorable biphotons. *Opt. Express*, 25(7):7300–7312, Apr 2017.

[6] Changchen Chen, Jane E. Heyes, Kyung-Han Hong, Murphy Yuezhen Niu, Adriana E. Lita, Thomas Gerrits, Sae Woo Nam, Jeffrey H. Shapiro, and Franco N. C. Wong. Indistinguishable single-mode photons from spectrally engineered biphotons. *Opt. Express*, 27(8):11626–11634, Apr 2019.

[7] Andreas Christ, Alessandro Fedrizzi, Hannes Hübel, Thomas Jennewein, and Christine Silberhorn. Parametric down-conversion. In *Experimental Methods in the Physical Sciences*, volume 45, pages 351–410. Elsevier, 2013.

[8] Chaohan Cui, Reeshad Arian, Saikat Guha, N. Peyghambarian, Quntao Zhuang, and Zheshen Zhang. Wave function engineering for spectrally-uncorrelated biphotons in the telecommunication band based on a machine-learning framework, 2019.

[9] L. Cui, X. Li, and N. Zhao. Spectral properties of photon pairs generated by spontaneous four-wave mixing in inhomogeneous photonic crystal fibers. , 85(2):023825, February 2012.

[10] P. Ben Dixon, Jeffrey H. Shapiro, and Franco N. C. Wong. Spectral engineering by gaussian phase-matching for quantum photonics. *Opt. Express*, 21(5):5879–5890, Mar 2013.

[11] Annamaria Dosseva, Łukasz Cincio, and Agata M. Brańczyk. Shaping the joint spectrum of down-converted photons through optimized custom poling. *Phys. Rev. A*, 93:013801, Jan 2016.

[12] Annamaria Dosseva, Łukasz Cincio, and Agata M Brańczyk. Shaping the joint spectrum of down-converted photons through optimized custom poling. *Physical Review A*, 93(1):013801, 2016.

[13] M. M. Fejer, G. A. Magel, D. H. Jundt, and R. L. Byer. Quasi-phase-matched second harmonic generation: tuning and tolerances. *IEEE Journal of Quantum Electronics*, 28(11):2631–2654, Nov 1992.

[14] Vittorio Giovannetti, Seth Lloyd, and Lorenzo Maccone. Quantum metrology. *Phys. Rev. Lett.*, 96:010401, Jan 2006.

[15] Francesco Graffitti, Peter Barrow, Massimiliano Proietti, Dmytro Kundys, and Alessandro Fedrizzi. Independent high-purity photons created in domain-engineered crystals. *Optica*, 5(5):514–517, May 2018.

[16] Francesco Graffitti, Jérémy Kelly-Massicotte, Alessandro Fedrizzi, and Agata M Brańczyk. Design considerations for high-purity heralded single-photon sources. *Physical Review A*, 98(5):053811, 2018.

[17] Francesco Graffitti, Dmytro Kundys, Derryck T. Reid, Agata Brańczyk, and Alessandro Fedrizzi. Pure single photon generation from nonlinear processes. Optical Society of America, 2017.

[18] Francesco Graffitti, Dmytro Kundys, Derryck T Reid, Agata M Brańczyk, and Alessandro Fedrizzi. Pure down-conversion photons through sub-coherence-length domain engineering. *Quantum Science and Technology*, 2(3):035001, 2017.

[19] David J Griffiths. Introduction to electrodynamics, 2005.

[20] Sten Helmfrid and Gunnar Arvidsson. Influence of randomly varying domain lengths and nonuniform effective index on second-harmonic generation in quasi-phase-matching waveguides. *J. Opt. Soc. Am. B*, 8(4):797–804, Apr 1991.

[21] Sten Helmfrid, Gunnar Arvidsson, and Jonas Webjörn. Influence of various imperfections on the conversion efficiency of second-harmonic generation in quasi-phase-matching lithium niobate waveguides. *J. Opt. Soc. Am. B*, 10(2):222–229, Feb 1993.

[22] C. K. Hong, Z. Y. Ou, and L. Mandel. Measurement of subpicosecond time intervals between two photons by interference. *Phys. Rev. Lett.*, 59:2044–2046, Nov 1987.

[23] Werner Känzig. Ferroelectrics and antiferroeletrics. In *Solid State Physics*, volume 4, pages 1–197. Elsevier, 1957.

[24] H. Karlsson. Frequency doubling in periodically poled rbtioaso¡sub¿4¡/sub¿. *Electronics Letters*, 32:556–557(1), March 1996.

[25] H. Karlsson and F. Laurell. Electric field poling of flux grown ktiopo4. *Applied Physics Letters*, 71(24):3474–3476, 1997.

[26] GD Miller. *Periodically Poled Lithium Niobate: Modeling, Fabrication, and Nonlinear-Optical Performance.* PhD thesis, Stanford University, 1998.

[27] C I Osorio, N Sangouard, and R T Thew. On the purity and indistinguishability of down-converted photons. *Journal of Physics B: Atomic, Molecular and Optical Physics*, 46(5):055501, feb 2013.

[28] J. S. Pelc, C. R. Phillips, D. Chang, C. Langrock, and M. M. Fejer. Efficiency pedestal in quasi-phase-matching devices with random duty-cycle errors. *Opt. Lett.*, 36(6):864–866, Mar 2011.

[29] Jason S Pelc, Carsten Langrock, Qiang Zhang, and Martin M Fejer. Influence of domain disorder on parametric noise in quasi-phase-matched quantum frequency converters. *Optics letters*, 35(16):2804–2806, 2010.

[30] Nicolás Quesada and Agata M. Brańczyk. Gaussian functions are optimal for waveguided nonlinear-quantum-optical processes. *Phys. Rev. A*, 98:043813, Oct 2018.

[31] Matteo Santandrea, Michael Stefszky, Vahid Ansari, and Christine Silberhorn. Fabrication limits of waveguides in nonlinear crystals and their impact on quantum optics applications. *New Journal of Physics*, 21(3):033038, mar 2019.

[32] Lynden K. Shalm, Evan Meyer-Scott, Bradley G. Christensen, Peter Bierhorst, Michael A. Wayne, Martin J. Stevens, Thomas Gerrits, Scott Glancy, Deny R. Hamel, Michael S. Allman, Kevin J. Coakley, Shellee D. Dyer, Carson Hodge, Adriana E. Lita, Varun B. Verma, Camilla Lambrocco, Edward Tortorici, Alan L. Migdall, Yanbao Zhang, Daniel R. Kumor, William H. Farr, Francesco Marsili, Matthew D. Shaw, Jeffrey A. Stern, Carlos Abellán, Waldimar Amaya, Valerio Pruneri, Thomas Jennewein, Morgan W. Mitchell, Paul G. Kwiat, Joshua C. Bienfang, Richard P. Mirin, Emanuel Knill, and Sae Woo Nam. Strong loophole-free test of local realism. *Phys. Rev. Lett.*, 115:250402, Dec 2015.

[33] J-L. Tambasco, A. Boes, L. G. Helt, M. J. Steel, and A. Mitchell. Domain engineering algorithm for practical and effective photon sources. *Opt. Express*, 24(17):19616–19626, Aug 2016.

[34] M. Yamada, N. Nada, M. Saitoh, and K. Watanabe. Firstorder quasiphase matched linbo3 waveguide periodically poled by applying an external field for efficient blue secondharmonic generation. *Applied Physics Letters*, 62(5):435–436, 1993.

APPENDICES

Appendix A

Sellmeier's equations

Sellmeier's equation describes the refractive index in a material for a specific wavelength or frequency. The parameters (A, B, C & D) used in it for a specific material can be experimentally extracted. Sellemeier's equation can be written in the following way:

$$n_i^2(\lambda) = A + \frac{B\lambda^2}{\lambda^2 - C} - D\lambda^2 \tag{A.1}$$

Equations (A.2) and (A.3) show the wavelength dependency of the two orientation (x and y) along the two polarization axis in KTP that were used for most simulations in this thesis.

$$n_x^2(\lambda) = 2.10468 + \frac{0.89342\lambda^2}{\lambda^2 - 0.04438} - 0.01036\lambda^2 \tag{A.2}$$

$$n_y^2(\lambda) = 2.14559 + \frac{0.87629\lambda^2}{\lambda^2 - 0.0485} - 0.01173\lambda^2 \tag{A.3}$$

where λ is the wavelength of light in vacuum. While a full description of dispersion in materials also require temperature, we assume that this degree of freedom is controlled and neglect the temperature as a factor.

Appendix B

Field correction for varying dispersions

It's possible to take in account the change of dispersions' effect on the PMF by changing the way of computing the PMF integral, adding a phase correction to each contributions of the individual domains. The original (unpoled) PMF equation,

$$\phi(\omega_s, \omega_i) = \int_0^L e^{i\Delta k z} dz, \tag{B.1}$$

can be solved using piece-wise integral adding each individual domain contributions to the PMF. In the case of a constant phase mismatch, we get:

$$\phi(\omega_s, \omega_i) = \sum_{n=0}^{N-1} \frac{e^{i\Delta k z_{n+1}} - e^{i\Delta k z_n}}{i\Delta k}. \tag{B.2}$$

with z_n being the position of the $(n+1)^{th}$ domain starting boundary. This will be incorrect in the case of a spatially varying Δk function, as each n^{th} term of the previous sum will be calculated as if the light went through the whole crystal with dispersion equations dictated by Δk_n (e.g the contribution of, say, the third domain will consider that the entering phase as it hits the third domain boundary is the one the incident beam would have if it travelled two domains with the same dispersion relations changing its wavelength in the third domain). A solution to solve this is to reformulate the previous equations to always add domain contributions as if they were the first domain, but multiply it by the phase which correct for the propagation through the previous segments (which for each segment is $e^{i\Delta k_n(z_{n+1}-z_n)}$). Taking account all of the previous domains, this phase factor θ would be, for the n^{th} index, (with $n > 0$):

$$\theta_n = \prod_{i=0}^{n-1} e^{i\Delta k_n \Delta z_n}. \tag{B.3}$$

Using this phase, we can rewrite the sum of equation *B.2* as a sum of single domains integrals of length Δz_n, separating the first domain which doesn't have a phase correction:

$$\phi(\omega_s, \omega_i) = \frac{e^{i\Delta k_0 \Delta z_0} - 1}{i\Delta k_0} + \sum_{n=1}^{N-1} \theta_n \frac{e^{i\Delta k_n \Delta z_n} - 1}{i\Delta k_n}. \tag{B.4}$$

This can be rewritten in the form that was used in [9] as

$$\phi(\omega_s, \omega_i) = \Delta z_0 sinc(\frac{\Delta k_0 \Delta z_0}{2}) + \sum_{n=1}^{N-1} \theta_n \Delta z_n sinc(\frac{\Delta k_n \Delta z_n}{2}). \tag{B.5}$$

If we want to add poling orientations to this equation, we add a ±1 factor to each segment contribution in equation B.3. The individual phase of the pump field is unaffected by the poling of the previous domains, so the poling only matters locally. We can simply add the poling for the domain n, which can be expressed in the phase factor directly:

$$\theta'_n = g(n) \prod_{i=0}^{n-1} e^{i\Delta k_n \Delta z_n}. \tag{B.6}$$

with g(n) being the poling orientation of the $(n+1)^{th}$ domain. With this correction, the full PMF would be given by

$$\phi(\omega_s, \omega_i) = g(0)\Delta z_0 sinc(\frac{\Delta k_0 \Delta z_0}{2}) e^{\frac{i\Delta k_0 \Delta z_0}{2}} + \sum_{n=1}^{N-1} \theta'_n \Delta z_n sinc(\frac{\Delta k_n \Delta z_n}{2}) e^{\frac{i\Delta k_n \Delta z_n}{2}}. \tag{B.7}$$

A number of papers dealing with varying dispersion relations in nonlinear medium (e.g [21]) uses a different expression, which reads:

$$\phi(\omega_s, \omega_i) = \int_0^L g(z) e^{i \int_0^z \Delta k(\epsilon) d\epsilon} dz. \tag{B.8}$$

This expression has practical advantages over equation B.7, but there are no formal derivation of it in literature that we are aware of. We have simulated both equations for different parameters and results have lead us to conclude that both expressions give the same resulting PMF.